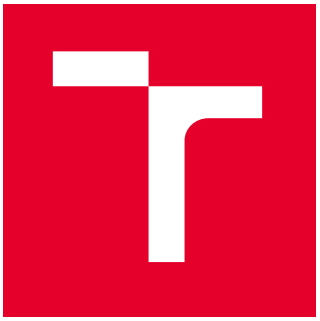

BRNO UNIVERSITY OF TECHNOLOGY

VYSOKÉ UČENÍ TECHNICKÉ V BRNĚ

FACULTY OF ELECTRICAL ENGINEERING AND COMMUNICATION

FAKULTA ELEKTROTECHNIKY
A KOMUNIKAČNÍCH TECHNOLOGIÍ

DEPARTMENT OF RADIO ELECTRONICS

ÚSTAV RADIOELEKTRONIKY

AN EASILY SCALABLE RECONFIGURABLE INTELLIGENT SURFACE PROTOTYPE

AN EASILY SCALABLE RECONFIGURABLE INTELLIGENT SURFACE PROTOTYPE

MASTER'S THESIS
DIPLOMOVÁ PRÁCE

AUTHOR
AUTOR PRÁCE

Bc. John Richard Ritter

SUPERVISORS
VEDOUCÍ PRÁCE

Dr. Robert Langwieser
TECHNISCHE UNIVERSITÄT WIEN

prof. Dr. Ing. Christoph Mecklenbräuker
TECHNISCHE UNIVERSITÄT WIEN

doc. Ing. Jaroslav Láčík, Ph.D.
VYSOKÉ UČENÍ TECHNICKÉ V BRNĚ

BRNO 2025

BRNO UNIVERSITY OF TECHNOLOGY
FACULTY OF ELECTRICAL ENGINEERING AND COMMUNICATION

Master's Thesis

Master's study program **Telecommunications (Joint Degree)**

Department of Radio Electronics

Student: Bc. John Richard Ritter ***ID:*** 211316

Year of study: 2 ***Academic year:*** 2024/25

TITLE OF THESIS:

An easily scalable reconfigurable intelligent surface prototype

INSTRUCTION:

The development of an improved and scalable RIS design based on previous work [1][2] is the aim of this thesis. The focus will be mainly on following aspects:

1) Scalability of the overall RIS surface so that individual modules can be mounted side by side to build up variable sizes of the RIS on a PCB base – frameless design.

2) Manufacture a RIS prototype and test its properties.

3) Implemetation and testing of the RIS controller for the scalable RIS design which requires to handle multiple D/A converters. The concept of the current RIS controller allows for such an extension [1], but was not implemented or tested.

4) Implemetation and testing of an upscaled RIS surface (e.g. two RIS PCBs).

RECOMMENDED LITERATURE:

[1] M. KERBLER; Control Unit for a Reconfigurable Intelligent Surface. Bachelor thesis. Wien: TU Wien. 2022.
[2] S. ZHAO; R. LANGWIESER; C. F. MECKLENBRÄUKER. Reconfigurable digital metasurface for 3-bit phase encoding. In: WSA 2021; 25th International ITG Workshop on Smart Antennas. 2021, pp. 1–6.

Date of project specification: 10.2.2025 ***Deadline for submission:*** 26.5.2025

Supervisor: doc. Ing. Jaroslav Láčík, Ph.D.
Consultant: Dipl.-Ing. Dr.techn. Robert Langwieser, Prof. Ing. Dipl.-Ing. Dr.-Ing. Christoph Mecklenbräuker

doc. Ing. Lucie Hudcová, Ph.D.
Chair of study program board

ABSTRACT

The aim of this thesis is to design, manufacture, and characterize an improved and scalable reconfigurable intelligent surface module based on previous work. The borderless geometry of the RIS modules enables side-by-side installation to construct up-scaled reconfigurable intelligent surfaces. Two RIS modules were manufactured and tested, and shown to be fully operational by measurements. At operation frequency 5 GHz, the reflection phase is tunable over a range of 326° with bias voltages ranging from 0 V to 9.5 V. The results are consistent across both RIS modules. An up-scaled RIS consisting of two modules was also constructed and measured, showing the same characteristics as a single module but with a much larger magnitude of steerable reflection. The functional and easy-to-use RIS modules may prove useful in answering many major questions in the field of reconfigurable intelligent surface research.

KEYWORDS

Reconfigurable intelligent surface, scalable RIS, RIS module, scalability, prototype.

RITTER, John Richard. *An easily scalable reconfigurable intelligent surface prototype*. Master's Thesis. Brno: Brno University of Technology, Faculty of Electrical Engineering and Communication, Department of Radio Electronics, 2025. Advised by Dr. Robert Langwieser and prof. Dr. Ing. Christoph Mecklenbräuker.

Author's Declaration

Author:	Bc. John Richard Ritter
Author's ID:	211316
Paper type:	Master's Thesis
Academic year:	2024/25
Topic:	An easily scalable reconfigurable intelligent surface prototype

I declare that I have written this paper independently, under the guidance of the advisor and using exclusively the technical references and other sources of information cited in the paper and listed in the comprehensive bibliography at the end of the paper.

As the author, I furthermore declare that, with respect to the creation of this paper, I have not infringed any copyright or violated anyone's personal and/or ownership rights. In this context, I am fully aware of the consequences of breaking Regulation § 11 of the Copyright Act No. 121/2000 Coll. of the Czech Republic, as amended, and of any breach of rights related to intellectual property or introduced within amendments to relevant Acts such as the Intellectual Property Act or the Criminal Code, Act No. 40/2009 Coll. of the Czech Republic, Section 2, Head VI, Part 4.

Brno ....

author's signature*

*The author signs only in the printed version.

ACKNOWLEDGEMENT

This thesis was created as part of the joint-degree study program Telecommunications organized by the Department of Radio Electronics at the Brno University of Technology and the Institute of Telecommunications at the TU Wien. I would like to thank everyone involved in the organization of this study program. Special thanks go to my advisors Dr. Robert Langwieser and prof. Dr. Ing. Christoph Mecklenbräuker for their valuable input.

Contents

List of Figures

1 Introduction

Wireless communication channels have always been considered uncontrollable. Wireless networks estimate channel properties before starting communication. When the channel is in a disadvantageous state for communication, the network has limited possibilities to work around it. *Reconfigurable intelligent surfaces* (RISs) are an emerging technology that promises control of the wireless channel. [1], [2]

They promise the ability to extend the coverage range of wireless networks, create virtual lines of sight between users and transmitters, increase localization and sensing precision, and much more, all while consuming little to no power. [2] Because reconfigurable intelligent surfaces interact directly with propagated signal waves, RIS technology will be highly compatible with existing and future communication schemes. The low manufacturing cost and low power consumption of reconfigurable intelligent surfaces mean that they can be used on almost any surface: walls, windows, billboards, vehicles, etc. [2], [3]

There is a strong theoretical foundation on RIS technology. However, the theoretical findings need experimental validation. RIS modeling, RIS-aided system modeling, RIS configuration optimization are all topics that need to be explored practically. [2], [4]

This thesis aims to create a scalable RIS prototype that allows further research on these topics. This RIS prototype can be used for experimental validation of theoretical findings in reconfigurable intelligent surface research.

The proposed RIS prototype is based on an existing prototype [5]. The existing design was reworked and redesigned to create a more versatile and scalable RIS design. The possibility to mount individual RIS modules side by side to create a larger RIS makes the design easily scalable. Two RIS modules based on the proposed design were manufactured and tested.

The structure of the thesis is the following. Chapter 2 provides a theoretical background to the topic of reconfigurable intelligent surfaces. The term RIS is defined. The operating principles and the construction of RISs are described. The system model of an RIS channel is introduced. The performance of RIS-aided communication is discussed. Lastly, some existing RIS designs and their findings are presented.

Chapter 3 describes the design process of the proposed RIS prototype. First, the starting point, the existing prototype, is described. Then the redesign procedure coupled with simulated results is shown. Afterwards, an overview of other design considerations and features, for example, mounting, is given. Lastly, two RIS modules and an up-scaled RIS are produced and tested in a designated testbed [6]. Finally, their results are discussed.

2 Theoretical background

2.1 Introduction to reconfigurable intelligent surfaces

The paradigm of RISs was established recently [7], [8]. The name RIS is a more general term that includes multiple ideas and designs [1]. The highest potential for RISs is in the domain of wireless communication and sensing networks, and the fundamentals originate in metasurface research [9], [10].

Metasurfaces are two-dimensional structures that realize various actions on an incident wave — e.g. absorption, filtering of frequency content or angles of incidence, polarization control, and anomalous reflections, to name a few. Historically, they have first been used in scenarios where the incident wave was known in advance and one specific response was desired. Metasurfaces are often constructed from a single unit cell that is periodically repeated on a given planar surface. The unit cell is designed to be small enough, so that the surface can be considered homogeneous and characterized by surface parameters such as the sheet impedance. The shape and resonant properties of the unit cell define the behavior of the resulting metasurface [10].

Since there was only one single use case for any given metasurface, the idea of a reconfigurable metasurface arose. The goal was to allow tunability of the surface with relatively simple means. Different concepts were proposed that could tune the properties of the whole surface. One of the simplest ways that also enables tuning of individual cells separately is using lumped voltage-controlled components like PIN-diodes or varactor diodes. The RIS was born [10].

As mentioned above, reconfigurable intelligent surfaces implement locally tunable metasurfaces that enable the creation of smart radio environments – their specific materials, structures, and geometric designs are open to the creativity of engineers [1]. However, most commonly they are realized as a patch-array-type reflective metasurface with unit cells that have tunable reflection properties by incorporating varactors and/or PIN diodes, cf. [1], [10], [11]. Their tunability enables RISs the shaping the electromagnetic wave propagation environment and the creation of controllable communication channels [1], [2].

RISs do not contain an RF chain [12] and have very low power consumption — in designs using varactor diodes only the circuit controlling the voltage on the diodes consumes any power. [11] This passivity coupled with the ability to reflect and beamform incident waves in a desired manner gives RISs some unique advantages [2], [3].

Easy to utilize – since RISs are nearly-passive and can be inexpensively manufactured, they can be easily utilized on walls, windows, vehicles, possibly even clothing.

Spectral efficiency – RISs "recycle" the existing electromagnetic waves and reflect them to a receiver; this way they can help compensate for power loss over long distances or create virtual line-of-sight links to said receiver, thus improving the *signal-to-interference-plus-noise ratio* (SINR).

Energy efficiency – compared to relaying systems (be it *amplify-and-forward* (AF) of *decode-and-forward* (DF)) RIS shapes and forms the incoming electromagnetic wave without using any power amplifiers making it more energy efficient.

Compatibility – RISs act as a normal reflector would and therefore support full-duplex transmission; they can also be incorporated into existing and/or future technologies and standards.

For their many capabilities, reconfigurable intelligent surfaces are usable in a variety of application scenarios. For example, in cellular networks they potentially decrease the power loss of signals, mitigate the interference of neighboring cells, and increase physical layer security by smartly configuring their beamforming. Indoors RISs are capable of eliminating spots without network coverage and increasing data throughput and connection reliability . They can even be used in networks that support automated vehicles or help in *Internet of Things* (IoT) applications [2].

In the remainder of this section, some nomenclature that is often used interchangeably with "RIS" is examined. The next section considers the physical construction of a RIS together with its operating principles. Later sections investigate channel models, RIS configuration optimization and integration of reconfigurable intelligent surfaces with machine learning and other technologies. Lastly, the landscape of existing RIS prototypes is investigated.

2.1.1 Different names for RISs

Since reconfigurable intelligent surfaces are a new paradigm that has not yet been standardized, many names are used somewhat interchangeably while they do not necessarily have the same meaning. Some of these are listed and explained below.

Intelligent reflective surface

Intelligent reflective surfaces (IRSs) are RISs that work as reflectors. [13] Most commonly reconfigurable intelligent surfaces are understood to be IRSs. [2] IRSs are a 1-port metasurface, which only reflects. This term can be used when it is necessary to specifically differentiate between RISs deployed as reflectors and not transmitters.

Intelligent transmitting surface

For an RIS that is used as a 2-port system, ergo a transmitting metasurface, the term *intelligent transmitting surface* (ITS) can be used. [13] This is a concept that is not as widely studied as its counterpart, the IRS. ITSs do have some interesting applications, such as being integrated into glass walls of buildings such as skyscrapers [13] or being part of a transmitarray antenna (mentioned below) [14].

Large intelligent surfaces

Large intelligent surfaces (LISs) have a similar goal to reconfigurable intelligent surfaces but they are different. The two differ in their architecture and operation. An LIS utilizes active components in its design and can receive and transmit impinging signals, similar to a relay. [15]

Programmable metasurfaces

Programmable metasurfaces, sometimes called coding metasurfaces, allow for the control of the metasurface in a discrete number of configurations / states. An example of this is an RIS tuned by PIN diodes. The discrete states of the metasurface can be coded into a bit sequence that can be handled by an *field programmable gate array* (FPGA) or similar. To increase the amount of discrete states multiple cells of a metasurface can be controlled as one entity or more actuators can be integrated into one cell. Metasurfaces that are tuned by lumped electronic components such as RISs can easily be made programmable. [10]

Software-defined metasurfaces

Software-defined metasurfaces (SDMs) are one step further from programmable metasurfaces. SDMs expand on the idea of programmable metasurfaces by replacing the actuators of the cells with controllers that are able to control the unit cell, sense the incident wave and communicate with one another. From a design perspective, accommodations for the controllers need to be made - this remains one of the main challenges of SDMs. [10]

Active RIS

One problem of RISs is the multiplicative fading effect. This effect is caused by the nature of the RIS path in the wireless channel. The RIS path is represented by three parts in cascade: the transmitter-to-RIS link, the RIS and the RIS-to-receiver link. The path loss of this cascade is given by the product of the individual path losses. When the direct path from transmitter to receiver is strong and unobstructed, the

signal from the RIS path is weak in comparison. In this case, the RIS would need a large number of unit cells to achieve noticeable increases in channel capacity. To combat this, active RISs have been proposed. Their unit cells are equipped with a reflection-type amplifier, which enables them to not only change the phase of the incident wave but also amplify it. When talking about active RISs, the conventional RIS is usually called a passive RIS for better distinction. [16]

Reflectarray antenna

Reflectarray antennas (RTAs) consist of two main parts: a feed source and an IRS. The source creates a wave that strikes the IRS which reflects the wave in a desired manner. Because the IRS consists of multiple cells arranged in an array and can be reconfigured, the construct works as an array antenna that forgoes the usually complex feed network of patch array antennas in favor of a spatial feed realized by the feed source. RTAs share a similar construction to parabolic antennas and also have the same problem of the feed blocking part of the scattered wave. An RTA is an active device and is therefore not the same as an RIS. [14]

Transmitarray antenna

Similar to RTAs, *transmitarray antennas* (TMAs) feature a feed source and a metasurface that work together as an antenna array. The source feeds the metasurface; this time an ITS is used, which then alters the incident wave to a desired scattered/transmitted wave. In contrast to RTAs, TMAs do not have the issue of feed blocking, since the feed does not occupy the same half-space as the scattered wave. TMAs are active devices and should therefore not be confused with RISs. [14]

2.2 RIS – physical aspect

In this section, we explore the physical aspects of an RIS. We first discuss two important ways an RIS can interact with and shape incident waves. We also mention that in order to achieve this, RIS needs to be locally tunable. Afterwards, different ways to achieve tunability are introduced. Lastly, a description of a typical RIS architecture together with its mathematical model is presented.

2.2.1 Interaction with EM waves

The two main abilities of an RIS in terms of how it interacts with an impinging wave are beam steering (anomalous reflection) and beam forming (beam focusing). [2] [10]

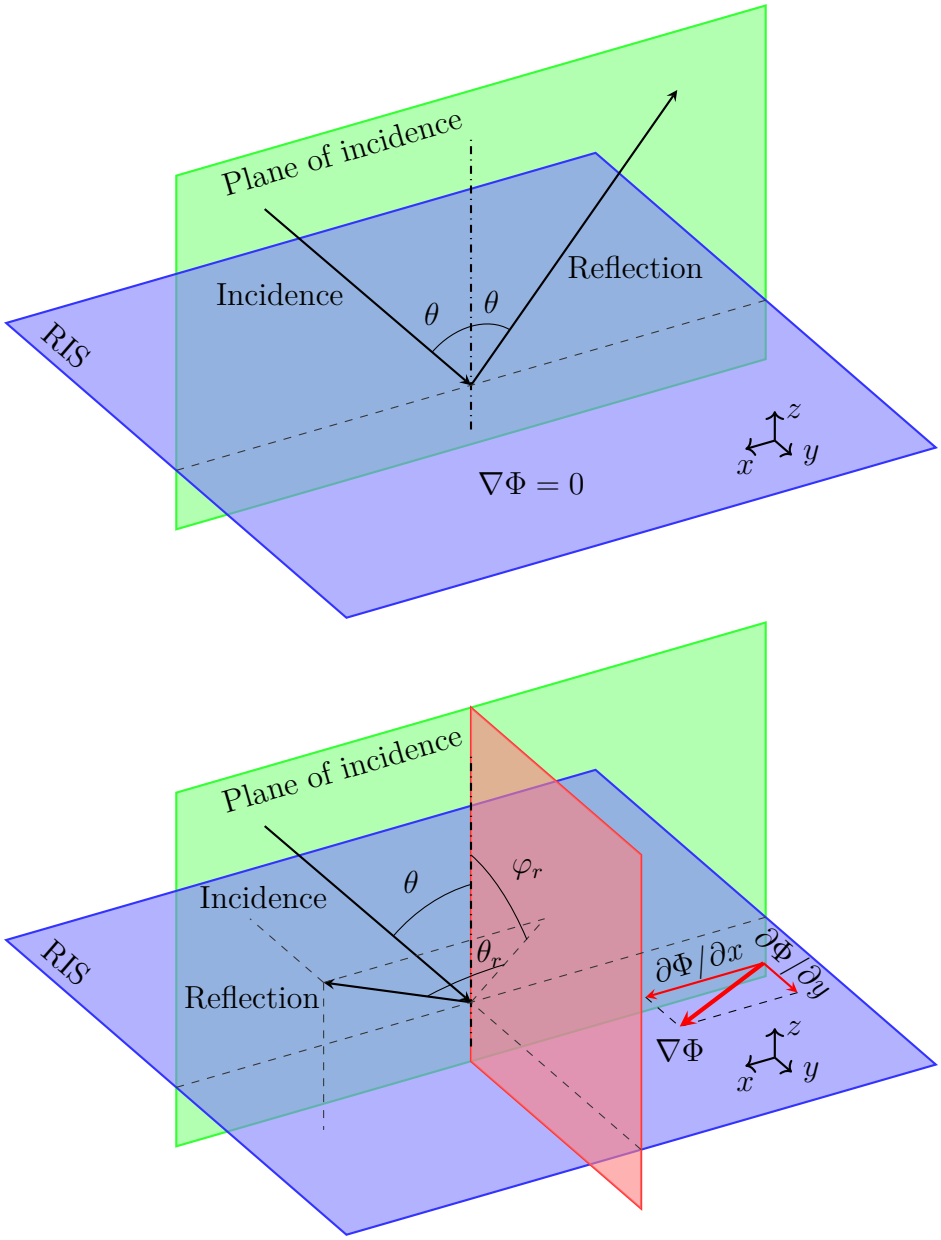

Fig. 2.1: Anomalous reflection showcased. The upper picture shows the scenario with zero phase gradient $\nabla\Phi = 0$ (all unit cells have the same reflection phase). The lower picture shows an anomalous reflection outside the plane of incidence when a phase gradient is present $\nabla\Phi \neq 0$.

Beam steering (anomalous reflection)

The first of the two important interactions is anomalous reflection, also called beam steering. Looking at the problem from the eyes of ray-optics, when a beam hits a boundary between two homogeneous materials with different refractive indices, it is reflected and refracted. In this case, the angle of reflection is the same as the angle of incidence. However, when this reflected angle is different from the incident angle, we speak of anomalous reflection. [2] The ability to steer the beam in an arbitrary direction allows RISs to service a specific receiver/user in a given direction.

Suppose that the boundary of the two materials is coated with an RIS that introduces phase discontinuities (given by the reflection coefficient of the unit cells). Using the generalized laws of reflection and refraction, it was found that the angle of reflection also depends on the gradient of the phase discontinuity $\nabla\Phi$ introduced at the boundary, ergo the RIS. [17] If the phase discontinuity gradient $\nabla\Phi$ is nonzero in both the direction of the plane of incidence ($\partial\Phi/\partial x$) and perpendicular to it ($\partial\Phi/\partial y$), the reflected beam can be steered into an arbitrary direction even outside of the plane of incidence. [17] On the other hand, if the phase discontinuity is the same for the whole surface, the angle of reflection remains unaltered. [17]

The effect of an RIS on the direction of the reflected beam is depicted in figure 2.1. Two scenarios are shown: one where the phase of the reflection coefficients of the unit cells is constant and the phase gradient is zero $\nabla\Phi = \vec{0}$ and the other for which the phase gradient is nonzero $\nabla\Phi \neq \vec{0}$.

Nearfield Beamforming

Nearfield beamforming, also known as beam focusing, is implemented by the RIS by concentrating the incident beams at a desired focal point. [2] This is similar to a parabolic mirror focusing electromagnetic waves on its focal point. Beam focusing is feasible when the source of the wave and/or the desired receiver is in the near-field region of the RIS [2]. In these cases, the phase differences associated with different rays to and from individual unit cells must be compensated by the phase of the unit cell's reflection coefficients. In this way, all rays arrive at the receiver with the same phase and interfere constructively.

In Ref. [18] this co-phase condition was derived for the case where the source is in the near-field, i.e.,

$$-k_0\left(|\vec{r}_{mn} - \vec{r}_s| - \vec{r}_{mn}\cdot\vec{u}_o\right) + \phi_{mn} = 2\pi l, \text{ with } l \in \mathbb{N}, \tag{2.1}$$

where $k_0 = 2\pi/\lambda$ is the free space wavenumber, $\vec{r}_{mn}$ is the position of the cell (m, n) in a $M \times N$ RIS array, $\vec{r}_s$ is the position of the source, $\vec{u}_o$ is the direction

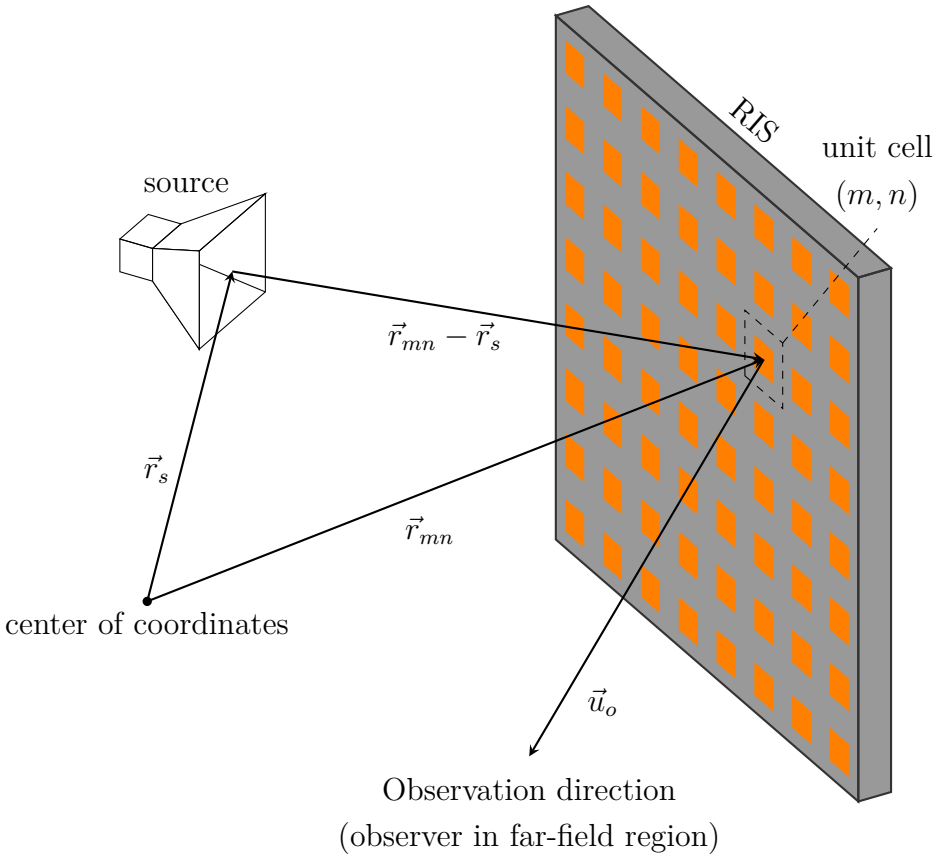

Fig. 2.2: Visualization of the co-phase condition that is required for effective beamforming. The scenario depicted is for a source in the near-field region with an observation point in the far-field region.

of the receiver (since it is in the far field in this scenario), and ϕ_{mn} is the phase difference caused by the RIS cell. The scenario is depicted in Fig. 2.2.

Application-specific requirements on an RIS

With these two principles, the configurations of RISs for future applications are derived in [2]. In this way, reconfigurable intelligent surfaces interacts with electromagnetic waves like a given object of the same size and arbitrary shape [1]. The potential use of an RIS is steering the beam from a source into the direction of a specified user when both are in the far-field region. When either the source or the receiver is in the near-field region (e.g., in a building) then focusing the wave on the source's and/or receiver's location is desired [2].

In order to carry out these tasks, an RIS needs to create a phase gradient on its interacting surface by incrementing or decrementing the reflection coefficients' phase between adjacent unit cells [2]. Therefore the RIS needs to be capable of

realizing specified reflection coefficients for each cell individually (or local groups of unit cells). This is called local tunability [10].

2.2.2 Tunability in metasurfaces

Tunability of a metasurface is achieved by introducing materials or components (e.g., varactor diodes) whose electromagnetic properties can be influenced by external stimuli. The particular stimulus needed varies according to the introduced variable element - it can range from temperature to electric and magnetic bias fields and voltage. With these stimuli, one can achieve the change of certain electromagnetic properties like permittivity, conductivity or impedance and thereby changing the response of the whole metasurface. [10]

Basic tuning affects the entire metasurface, all unit cells, in the same way. For that reason, the term *global tuning* is used. On the other hand, *local tuning* provides the capability to tune individual cells or small groups independently of each other. [10]

Next, some global tuning mechanisms are briefly mentioned. After that, the link between these mechanisms and local tunability and, ultimately, reconfigurable intelligent surfaces is explored.

Electro-optical tuning

Electro-optical tuning exploits the effect that a low-frequency electric field ("electro") in a material acting as a wave propagation medium affects the high-frequency ("optical") properties of the material. Often, this is realized by applying a voltage between electrodes to create the electric field. The most common materials used for electro-optical tuning are liquid crystals and graphene [10].

Optical tuning

The material is illuminated by light and changes its dielectric properties: this is known as optical control of dielectric permittivity [19], [20]. Light-sensitive semiconductors and graphene can be used for their ability to change their electromagnetic properties when illuminated. On the other hand, materials that change their mechanical properties when exposed to the right optical stimulus can also be used, e.g. in capacitor-like structures to change the capacitance. [10]

Magnetic tuning

One of the most thoroughly studied ways to achieve magnetic tunability is the ferromagnetic resonance occurring in ferrite materials. The characteristics of the

resonance are given by the ferrite material itself and an applied magnetic bias field. Although ferrites are the most prevalent, structures without them have been proposed. These include THz metamaterials, filters with semiconductor resonant structures and bioinspired microplate arrays. [10]

Thermal tuning

Heat is another way to achieve tunability. Phase-change materials feature a phase change that is dictated by the temperature - vanadium oxide has a metal-to-insulator phase change, with the transition happening close to room temperature. Semiconductors and superconductors can also be used, but their sensitivity to temperature is not high. [10]

Voltage-controlled lumped element tuning

Lumped electronic components that change their impedance based on an applied DC bias voltage provide a powerful way to realize tunability in metasurfaces. [10] The most prevalent components used in regards to RISs are PIN-diodes and varactor diodes. [1] [2].

Local tunability

In the text above, multiple ways to achieve tunability are mentioned. All of them can be used to tune the whole metasurface, achieving global tunability. [10] As was previously mentioned, for an RIS to function properly, the metasurface needs to be locally tunable.

All of the mentioned approaches to tunability can be adapted for local tuning. However, the easiest approach is to use voltage-controlled components. [10]

With PIN or varactor diodes the biasing circuit just needs to be designed to address every unit cell separately. This method avoids cross-talk and can even be used for a programmable integration. PIN diodes naturally have only two states of operation and for varactor diodes a set amount of used reverse bias voltages can be used; the states then can be expressed by means of binary codewords. [10]

2.2.3 RIS - construction

In this thesis, so far the concept of reconfigurable intelligent surfaces was introduced together with requirements that a RIS shall fulfill. In the following, the physical construction and corresponding mathematical model are discussed.

Physical construction

The RIS is a periodic patch array, truncated to fit on a finite surface connected to controllable lumped elements [1], [10], [11]. The unit cell of the periodic patch-array can be chosen quite freely, but square unit cells appear to be most common in the literature, [2]. The patch shapes vary depending on individual designs and use cases: cross-shaped [21], windmill-like [22], dumbbell-like shapes [23] have all been proposed. In [24] the authors designed a generative model that designs RIS patches using deep learning.

Often, the controllable elements for tuning the RIS are PIN switch diodes or varactor diodes [2], [10]. PIN diodes can be used in their "ON" state when forward-biased or in their "OFF" state when reverse-biased. This switchlike behavior is used to create a binary configuration - e.g. the cell fully absorbs or fully reflects, the phase of the reflection coefficient is switched between two values that are, ideally, π rad apart. [10] Varactor diodes are used as tunable capacitors because their reactance changes based on the applied reverse bias voltage. Their capacitance can be tuned continuously in an interval of approximately 0.5 to 5 pF with voltages 0 to 20 V. [10] The proposed prototype in this thesis uses varactor diodes as controllable elements.

The fact that RISs are patch arrays with readily available voltage-controlled elements creates the opportunity for easily realizable designs. [2] However, to work properly reconfigurable intelligent surfaces need biasing circuits and controllers (FPGA or similar) to control the diodes. [1] [11] Thanks to the nature of diode biasing, it is possible to design these biasing networks without crosstalk, which means that each cell is controlled independently from all others. [10]

The biasing networks, together with the diodes, consume some amount of power. Because of this, reconfigurable intelligent surfaces are not completely passive and their energy efficiency is also dependent on this power consumption. [11]

This is the core architecture of an RIS (depicted in figure 2.3). Other controllers or connections can be added to the RIS to create *channel state information* (CSI) channels or similar, expanding the architecture of an RIS according to its particular use case. [4]

Mathematical representation

As discussed, unit cells of an RIS can be individually controlled. Since unit cells are of sub-wavelength size and do not have active components, they are assumed to be passive circuits with impedance Z_l. When modeling RISs in wireless communication systems (without considering mutual coupling), each cell can be equivalently modeled with a reflection coefficient. The reflection coefficient for the cell (m, n) can be represented as: [2]

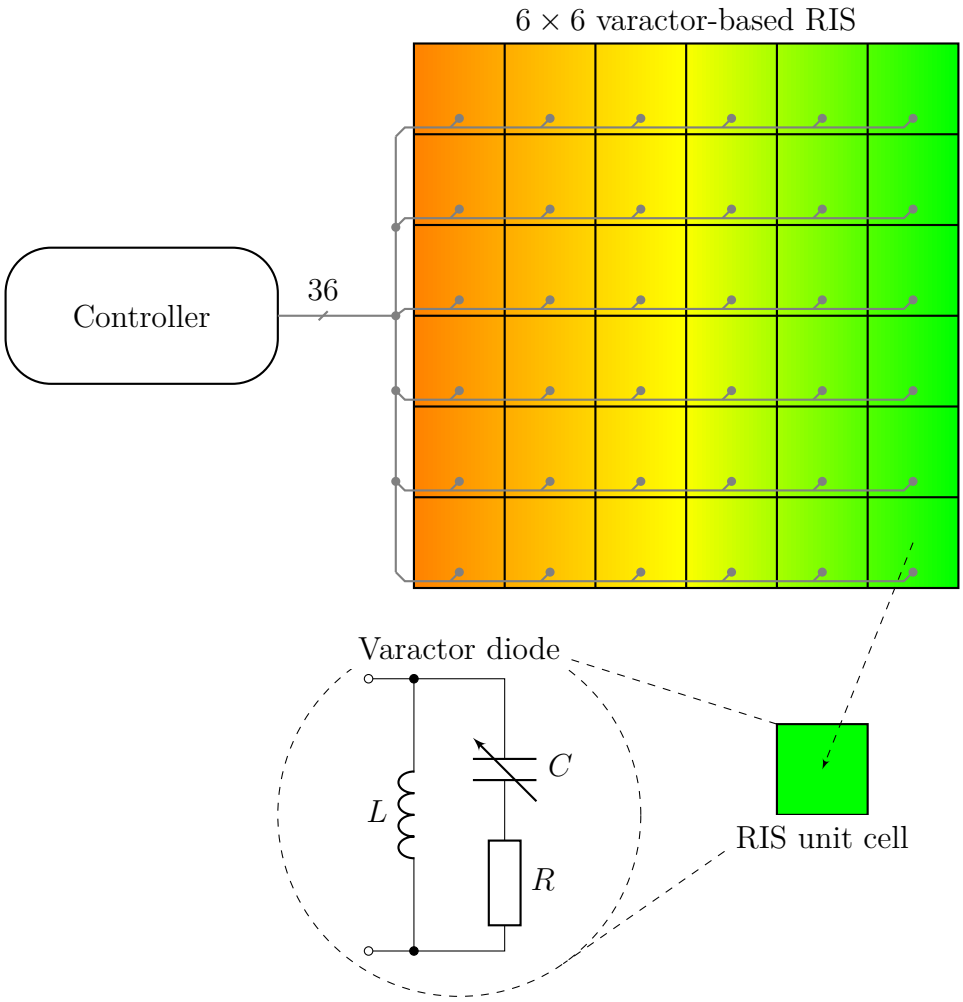

Fig. 2.3: Physical architecture of a varactor-based RIS. The RIS is divided into unit cells that all contain a varactor diode acting as a variable capacitor. All unit cells are individually connected to a controller that sets the biasing voltages for the varactor diodes.

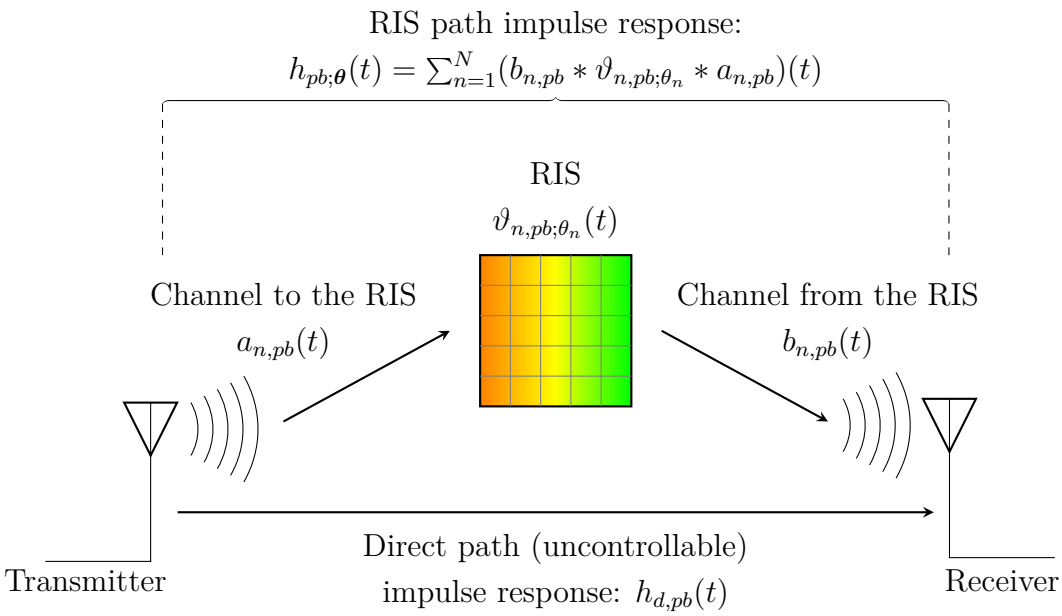

Fig. 2.4: System model of an RIS-aided communication SISO system

$$r_{mn} = \beta_{mn} \cdot e^{j\phi_{mn}}, \tag{2.2}$$

where β_{mn} is the amplitude response, ϕ_{mn} is the phase response, and j is the imaginary unit.

The amplitude and phase response are often assumed to be independent of each other in mathematical representations [2], but in reality they will always be dependent on each other and cannot be decoupled. [25] Moreover, the reflection coefficient also depends on the mutual coupling of the cells, which in many cases cannot be ignored. [2] Mathematical modeling of an RIS compliant with the actual behavior remains one of the open research issues. [3]

2.3 System model of RIS channel

2.3.1 End-to-end system model

In this part, the end-to-end system model for a SISO channel scenario with an RIS with N unit cells from [1] is presented (depicted in figure 2.4). Based on the system model presented, some assumptions and limitations will be discussed.

We consider a single antenna transmitter that sends a passband signal $x_{pb}(t)$ to a receiver using an RIS with N unit cells - SISO channel with an RIS present.

Firstly, when only the uncontrollable part of the channel is considered (the path in the lower part of figure 2.4), the received signal can be described as

$$y_{pb}(t) = (h_{d,pb} * x_{pb})(t) = \int_{-\infty}^{\infty} h_{d,pb}(u) x_{pb}(t-u) du. \tag{2.3}$$

In this case, the uncontrollable channel is modeled as linear and time-invariant (LTI) with impulse response $h_{d,pb}(t)$. $*$ is the convolution operator. This model holds as long as the impulse response of the channel does not change - for example, for one configuration of the RIS.

Now suppose that the transmitted real-valued passband signal $x_{pb}(t)$ is generated from a complex-valued baseband signal $x(t)$ with bandwidth $B/2$ modulated with carrier frequency f_c. The passband signal can be expressed as

$$x_{pb}(t) = \mathfrak{R}\left(\sqrt{2}x(t)e^{j2\pi f_c t}\right) = \frac{x(t)e^{j2\pi f_c t} + x^*(t)e^{-j2\pi f_c t}}{\sqrt{2}}, \tag{2.4}$$

where $\mathfrak{R}(\cdot)$ denotes the real part of a complex number, j is the imaginary unit. The relation in equation 2.4 can also be expressed in the frequency domain by taking its Fourier transform $\mathcal{F}(\cdot)$:

$$X_{pb}(f) = \frac{X(f-f_c) + X^*(-f-f_c)}{\sqrt{2}} \tag{2.5}$$

For convenience, a baseband representation of the signal relations is desired. Here, a pseudobaseband representation is introduced, where the received pseudobaseband signal $y(t)$ is defined similarly to the transmitted signal, meaning $y_{pb}(t) = \mathfrak{R}\left(\sqrt{2}y(t)e^{j2\pi f_c t}\right)$. Taking the Fourier transform of equation 2.3 and substituting for $X_{pb}(f)$ from equation 2.5 we get

$$\begin{aligned}
Y_{pb}(f) &= H_{d,pb}(f) \cdot \frac{X(f-f_c) + X^*(-f-f_c)}{\sqrt{2}} && (2.6)\\
&= \frac{H_{d,pb}(f)X(f-f_c) + H_{d,pb}(f)X^*(-f-f_c)}{\sqrt{2}} && (2.7)\\
&= \frac{H_{d,pb}(f)X(f-f_c) + H^*_{d,pb}(-f)X^*(-f-f_c)}{\sqrt{2}} && (2.8)\\
&= \frac{Y(f-f_c) + Y^*(-f-f_c)}{\sqrt{2}}. && (2.9)
\end{aligned}$$

In the second to last part of the equality the property $H_{d,pb}(f) = H^*_{d,pb}(-f)$ is used - this holds for real-valued passband signals. From this equation, it can be deduced that

$$Y(f-f_c) = H_{d,pb}(f)X(f-f_c) \Rightarrow Y(f) = H_{pb}(f+f_c)X(f). \tag{2.10}$$

Taking the inverse Fourier transform of this relation leads to the following

$$y(t) = (h_d * x)(t) = \int_{-\infty}^{\infty} h_d(u)x(t-u)du, \tag{2.11}$$

where $h_d(t) = h_{d,pb}(t)e^{-j2\pi f_c t}$ is the pseudobaseband equivalent of the passband impulse response $h_{d,pb}(t)$. The prefix *pseudo-* is given by the fact, that the impulse response $h_{d,pb}(t)$ is only frequency shifted to the baseband and is not a baseband filter.

RIS path system model

Now, the controllable path of the RIS is investigated. For each unit cell, the path has to be considered separately.

The transmitted signal first has to travel to the RIS through a channel with an impulse response $a_{n,pb}(t)$. The subscript n exemplifies the n-th unit cell of the RIS. The unit cell then interacts with the signal. Since cells are comparatively smaller than the signal wavelength and are passive, they can be modeled as LTI filters with impulse response $\vartheta_{n,pb;\theta_n}(t)$. θ_n is the tuning parameter (voltage applied to the varactor diodes) for the n-th RIS cell taken from the parameter vector $\boldsymbol{\theta} = [\theta_1, \theta_2, \ldots, \theta_N]^T$ (for a varactor-based design $\boldsymbol{\theta}$ is a voltage vector). Lastly, the signal then travels from the RIS to the receiver through an LTI channel with impulse response $b_{n,pb}(t)$.

For each cell, the path is a cascade of three LTI channels, which means that the overall impulse response $h_{n,pb}(t)$ is a convolution of their respective impulse responses - $h_{n,pb}(t) = (b_{n,pb} * \vartheta_{n,pb;\theta_n} * a_{n,pb})(t)$. The received signal is the sum of the signals from all the unit cell paths:

$$y_{pb}(t) = \sum_{n=1}^{N} \left(b_{n,pb} * \vartheta_{n,pb;\theta_n} * a_{n,pb} * x_{pb}\right)(t) \tag{2.12}$$

$$= \left(\left[\sum_{n=1}^{N} b_{n,pb} * \vartheta_{n,pb;\theta_n} * a_{n,pb}\right] * x_{pb}\right)(t), \tag{2.13}$$

where the sum in the square brackets is the impulse response of the RIS channel $h_{pb;\boldsymbol{\theta}}(t)$.

Similarly to the case of the uncontrollable channel, a pseudobaseband representation can be found. Here

$$y(t) = \left(\left[\sum_{n=1}^{N} b_n * \vartheta_{n;\theta_n} * a_n\right] * x\right)(t), \tag{2.14}$$

while once again the channel impulse responses in the pseudobaseband are just their frequency shifted passband variant: $a_n(t) = a_{n,pb}(t)e^{-j2\pi f_c t}$, $b_n(t) = b_{n,pb}(t)e^{-j2\pi f_c t}$,

$\vartheta_{n;\theta_n}(t) = \vartheta_{n,pb;\theta_n}(t)e^{-j2\pi f_c t}$. The impulse response $h_{\boldsymbol{\theta}}(t)$ for the entire RIS path is given by the sum of the individual impulse responses from equation 2.14.

2.3.2 RIS-aided communication

The modeling for this section is taken once again from [1] since it is a nice simplified example.

As was shown above, the communication system with one RIS can be modeled in the pseudobaseband through a collective impulse response $h_{\boldsymbol{\theta}}(t)$. The transmitted signal is altered by this impulse response before arriving at the receiver. When expressed with a discrete-time representation, the received signal is

$$z[k] = h_{\boldsymbol{\theta}} x[k] + w[k]; \quad k = 0, 1, 2, \ldots \tag{2.15}$$

Here $z[k]$ represents the received signal mentioned above, $h_{\boldsymbol{\theta}}$ is the discrete-time version of the channel impulse response (single complex value), $x[k]$ is the transmitted signal in discrete time, and $w[k]$ is the added noise, considered to be *additive white Gaussian noise* (AWGN) $w[k] \sim \mathcal{N}_{\mathbb{C}}(0, N_0)$.

Further assumptions must be made to arrive at a representation of an AWGN channel. First, the impulse response $h_{\boldsymbol{\theta}}$ needs to be constant for all symbols - this resembles the channel not changing during one transmission sequence. Next, we assume that the symbol rate of the transmitter is B and its power limit is P. Then one symbol has to satisfy the constraint $\mathbb{E}\{|x[k]|^2\} \leq P/B$. Lastly, the transmitter must have knowledge of the *signal-to-noise ratio* (SNR) - that is, the transmitter must know the state of the channel including the RIS. The SNR is given by $\mathrm{SNR} = P|h_{\boldsymbol{\theta}}|^2/(BN_0)$.

Under these assumptions, the channel capacity is

$$C = B\log_2(1 + \mathrm{SNR}) = B\log_2\left(1 + \frac{P|h_{\boldsymbol{\theta}}|^2}{BN_0}\right). \tag{2.16}$$

2.3.3 Configuring the RIS

In the previous two subsections an end-to-end system model for an RIS-aided SISO channel from [1] and a closed-form expression of the channel capacity have been introduced.

To maximize the capacity C, the optimal RIS configuration needs to be found and set. This is done first by estimating the uncontrollable portions of the channel, then by calculating the optimum RIS configuration (finding the optimal parameter $\boldsymbol{\theta}$) and lastly controlling the RIS and setting the aforementioned configuration. [1] [2] [4]

Channel estimation

Efficient and precise channel estimation is crucial for wireless communication systems. The ability to estimate the channel well depends greatly on the channel model used. If an inappropriate model is selected, the channel estimation is less descriptive of the actual state of the channel. [4] Since RISs pioneered the paradigm of controllable wireless environments, channel modeling needs to be introduced anew. [4] Even the well-known Shannon capacity formula in its conventional formulation needs to be revisited, because the system with an RIS is controllable. [3] Currently there are three main categories of channel models: path loss models, spatial models and small scale fading models. [2] Every approach has its merits. However, channel models remain an open research question that needs experimental validation. [2]

In addition to the appropriate channel models, estimation procedures and CSI channels need to be present. [4] Channel estimation procedures need to be introduced so that the communication system can estimate the channel and then distribute this information to the transmitter and users. [4] The individual paths in the channel are all best estimated separately, so the most optimal configuration of the RIS can be found. [4] In the system model introduced above (see figure 2.4), that would involve estimating the direct link impulse response $h_{d,pb}(t)$ and the individual to and from RIS cell impulse responses $a_{n,pb}(t),\ b_{n,pb}(t),\ \forall n = 1, 2, \ldots, N$. The RIS path impulse response $h_{\boldsymbol{\theta}}(t)$ can not be estimated as a whole, since the RIS configuration is decided from the estimated channel.

Configuration optimization

The next step after channel estimation is to find the optimal configuration of the RIS — represented by the stimulus $\boldsymbol{\theta}$. The success of this optimization greatly depends on the quality of the channel estimate. [4] The RIS configuration can be optimized for different purposes. The most straightforward method is to optimize for channel capacity. Other optimization goals can be minimal transmission power needed, energy efficiency, spectral efficiency and maximum sum rate and user fairness for system with multiple users. [2] An interesting use case for which the RIS can be configured is signal cancellation at a user. This could be used near cell edges in cellular networks or as a jamming method to avoid eavesdropping. [2]

The optimization problems are usually not easily solved. In [8] it was shown that for energy efficiency optimization leads to a non-convex problem that cannot be differentiated. Numerical methods and other simplifying approaches are taken to solve these problems. [2] Some methods lead to near-optimal solutions or can even theoretically find optimal solutions, but they are computationally very complex. [2] The choice of method is greatly dependent on the optimization problem posed. The

communication system (SISO channel, NOMA, OFDM, ...) and also the optimization goal (enhancing channel capacity, spectral efficiency, energy efficiency, jamming, ...) influence this choice greatly.[2]

Although great progress has been made in terms of the theoretical foundation of configuration optimization, experimental validation is needed to confirm the findings.[2] [4]

RIS control

With the channel estimated and the optimal configuration of the RIS found, what remains is to configure the RIS. For that, a designated control channel needs to be established. The control channel can be in-band or out-of-band. An in-band channel is sent in the same frequency band as the payload and therefore lowers the usable channel capacity. In addition, an in-band control channel would need the RIS to not only reflect signals but also to receive and decode control information. This means that additional components would need to be introduced, making the RIS more complex. [1]

Out-of-band control channels, on the other hand, do not consume part of the channel capacity, but they need their own separate communication channel, be it wired or wireless. In these cases, the RIS itself remains the same, but the systems that handle control information are added to the controller of the RIS.[1]

2.3.4 System performance enhancement with an RIS

Reconfigurable intelligent surfaces are introduced to wireless communication systems to enhance their performance. RISs allow for "recycling" of existing electromagnetic waves that would otherwise have gone unused. [3]

When talking about channel capacity or spectral efficiency, the performance boost caused by the RIS is dependent on the circumstances of the given system. When there is no *line-of-sight* (LOS) connection, the RIS significantly enhances system performance by creating virtual-LOS connections through anomalous reflection and beam steering; an adequate RIS placement is paramount in this case. [3] On the other hand, if there is a strong LOS link from the transmitter to the receiver, the impact of the RIS is less pronounced. This is due to the multiplicative fading effect, which is caused by the cascade of channels on the RIS-path. [16]

To explain the multiplicative fading effect we make use of the RIS system model introduced in Section 2.3.1 (see figure 2.4) and assume narrowband channels (the frequency response of the channel is constant for all relevant frequencies), the optimal RIS configuration and identical impulse responses $a_{n,pb}(t)$ and $b_{n,pb}(t)$ for all N unit cells of the RIS. The authors of [1] concluded that for this case the square

of the RIS-path impulse response modulus $|h_{\boldsymbol{\theta}}|^2$ that directly impacts the SNR (see equation 2.16) is equal to

$$|h_{\boldsymbol{\theta}}|^2 = \left| \sum_{n=1}^{N} \sqrt{\alpha_n \beta_n |\vartheta|} \right|^2 = N^2 \alpha \beta |\vartheta|, \tag{2.17}$$

where α and β are the modulus of the transmitter-to-RIS and RIS-to-receiver channels respectively and $|\vartheta|$ is the amplitude response of RIS. Multiplicative fading is caused by cascading of the three channels and is shown in the multiplication $\alpha \cdot \beta \cdot |\vartheta|$. This product is generally a very small number, which causes the RIS-path to be weak for low numbers N of unit cells. The term N^2 in the equation 2.17 means that physically large RISs with a higher number of cells are more effective. [1] [16]

Reconfigurable intelligent surfaces are often compared to relays. [2] This is an appropriate comparison, since both relays and reconfigurable intelligent surfaces are similarly placed into the environment and coordinate with the transmitter. [3]

In [8] an AF relay was compared to an RIS in an otherwise identical setup. The AF relay had the same number of antennas as the RIS had unit cells throughout the comparison. The authors found that the relay was undoubtedly more effective in terms of spectral efficiency (the amount of bits per second per hertz of frequency). The main reason for this is the transmitted power of the relay P_R. The RIS can only reflect a fraction of the transmission power P, but the relay always transmits with the same power P_R. The gap got smaller as P increased, because the relay power P_R becomes less relevant compared to the transmission power. However, a relay-aided system can be outperformed by an RIS-aided system in terms of spectral efficiency when the number of unit cells N of the RIS is sufficiently higher than the number of antennas of the relay. [2] For energy efficiency, the RIS seemed to be superior to the AF relay. This is caused by the power consumption of the relay being much higher than that of the nearly passive RIS. [8]

2.4 RIS implementations and prototypes

This section concerns itself with proposed RIS designs that are just simulated or even experimentally validated. The text will be structured as an assortment of different publications and their designs and findings will be mentioned. Lastly, there is a quick summary of the landscape of RIS prototypes and how it relates to the design proposed in this thesis.

The authors of [21] proposed an RIS design that works for three distinct frequency bands at 3 GHz, 5.2 GHz and 6.2 GHz. The chosen lumped elements are varactor diodes that are utilized in the range from 0.063 pF up to 0.275 pF. The unit cells are square with a side length of 13 mm and have two copper layers on

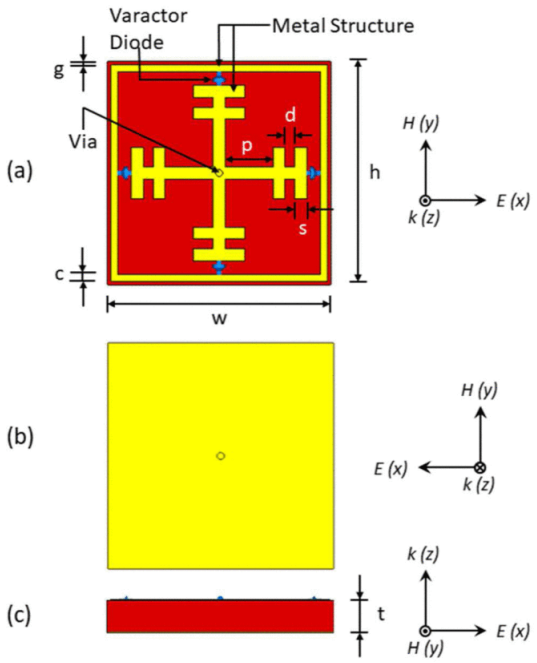

Fig. 2.5: RIS unit cell figure taken from [21]. (a) top view, (b) bottom view and (c) side view.

a Rogers substrate of thickness 1.57 mm. The bottom layer is used as the ground plane. Meanwhile, the top layer features a cross shape connected to a square ring with the diodes. In this configuration, each unit cell has 4 varactor diodes. For their simulation setup, the authors considered an RIS-array spanning 20 by 20 unit cells. The RIS was illuminated by an antipodal Vivaldi antenna positioned 86 mm above the RIS. The simulation results show that the proposed design works for all three frequency bands with varying peak gains and beam steering capabilities. For the 6.2 GHz band the RIS enhances the gain by 11 dBi and is capable of beam steering up to $\pm 75°$ with approximately 40% efficiency (7.1 dB loss). No prototype was constructed to be experimentally validated.

A reconfigurable intelligent surface with a large relative bandwidth was introduced in [23]. The design features a 4-layer stackup with the top 2 layers presenting the actual high frequency portion. Unit cells consist of two patches connected by a PIN diode - together they resemble a dumbbell. One patch is connected to ground, the other to a biasing voltage controlled by an FPGA. Unit cells have two states corresponding to the PIN diodes "on" and "off" states. These states have a $180° \pm 30°$ phase shift from one another in the frequency interval 15.5 - 27.5 GHz. The working frequency is set at 21.5 GHz, the arithmetic mean of the interval borders. An array of 18 by 18 unit cells was simulated to have a relative 3-dB gain bandwidth of 39.1%. The authors compared their work with similar works in terms of bandwidth

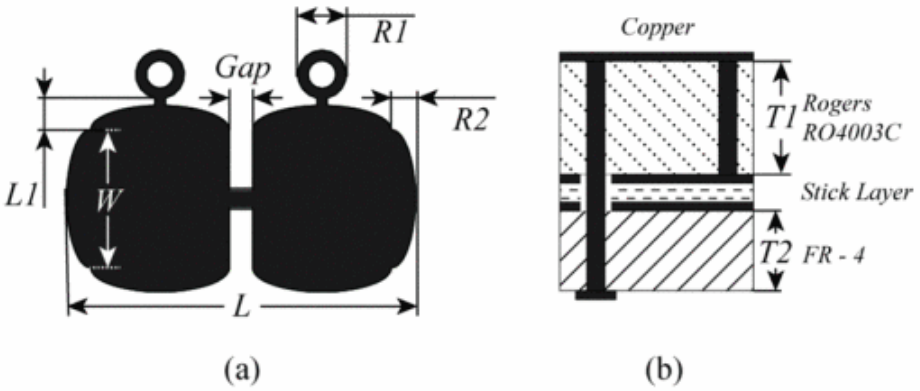

Fig. 2.6: RIS unit cell figure taken from [23]. (a) top view of patch, (b) layer stackup.

and concluded that they achieved the highest relative bandwidth. No prototype was constructed, no experimental validation was done.

The authors of [26] introduce a notable example of an active reconfigurable intelligent surface. The design was proposed, simulated and experimentally tested with a good match between simulations and measurements. The unit cells are hexagonal and feature a square patch. The RIS operates at 25.8 GHz. The cells have two ports, one for horizontally polarized waves and one for vertically polarized waves. These two ports are connected to an *field effect transistor* (FET) amplifier - vertical polarization as input and horizontal polarization as output. Then by controlling the bias voltages at the gate U_G and the drain U_D the authors were able to achieve four different unit cell states. The first two states were in what was called the reflective mode. The modulus of the reflection coefficient Γ_m was the same, but the phase was different. $\Gamma_m \in \mathcal{A}_\mathcal{R} = \{(0.4\angle 0°), (0.4\angle 67°)\}$. The other mode was called active mode and the reflection coefficient differed in the modulus - this corresponds to the amplifier being "on" and "off". $\Gamma_m \in \mathcal{A}_\mathcal{A} = \{(2\angle 0°), (0\angle 0°)\}$. The two states in the reflective mode would ideally differ by 180°, but due to the design being optimized for the active mode, the phase difference is less. In the measurements, it was found that the active mode offers better signal strength at the receiver compared to the reflective mode by about 12 dB. In both cases, specular reflection of the incident signal is also present. The reason is similar in both cases. For the reflective mode the smaller phase difference renders the RIS unable to avoid specular reflection and for the active mode to be able to avoid it a tunable phase would be required - the two states in active mode would also need to differ in phase by 180°. [26]

An approach to RIS design that aims to simplify configuration optimization is presented in [15]. This is done by making the unit cells have a preset reflection

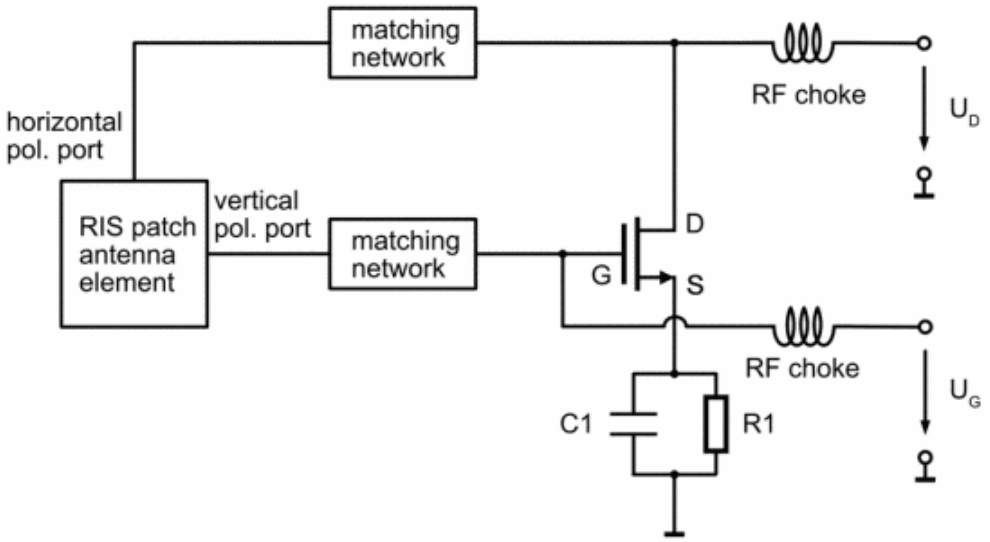

Fig. 2.7: RIS unit cell circuit diagram from Radpour et al. [26].

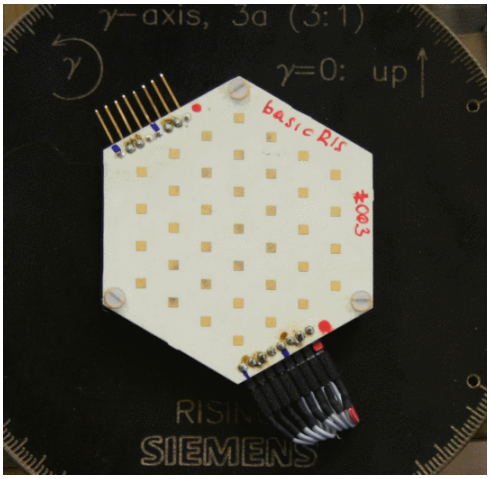

Fig. 2.8: Manufactured RIS installed in the measurement apparatus [26].

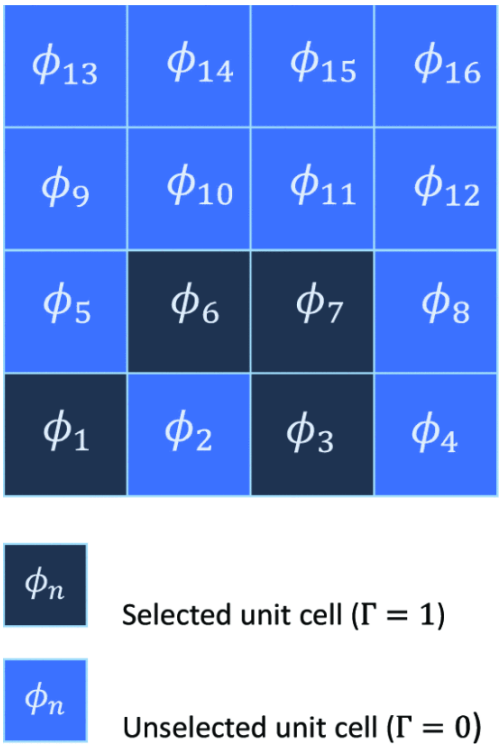

Fig. 2.9: Illustration of the operation principle of the RIS in [15].

phase ϕ_n that does not change. The reflection phases ϕ_n of the cells are different for all cells. Each cell has two states. In the first state, the cell reflects with its preset phase ϕ_n and in the second it acts perfectly absorptive. The simplification of the optimization is given by the constraint of the RIS design - the phases cannot be changed, the cells can only be turned "on" (reflective state) or "off" (absorptive state). Therefore, optimization reduces to finding the selection of the best K cells to be turned "on". The number K is decided beforehand. In the simulation, the authors used RISs with different array sizes (20×20, 30×30, 40×40) and investigated their performance with varying K. It was found that a 20×20 array with $K = 100$ chosen cells has performance similar to a reconfigurable intelligent surface with 100 fully reconfigurable cells. This, of course, comes at the price of having 300 unused cells in any given configuration. No prototype was created and no real-world measurements were made.

In [27] a scalable RIS design is introduced. The authors propose, simulate and measure their RIS with operation frequency 2.4 GHz in multiple scenarios. The RIS unit consists of a 4×4 array of unit cells controlled by a connected controller. Each RIS has its own controller on board and the control channel for the RISs is realized by an *radio-frequency identification* (RFID) network. The unit cells feature a 4-layer stackup: the two upper layers are stacked patches with auxiliary parasitic elements,

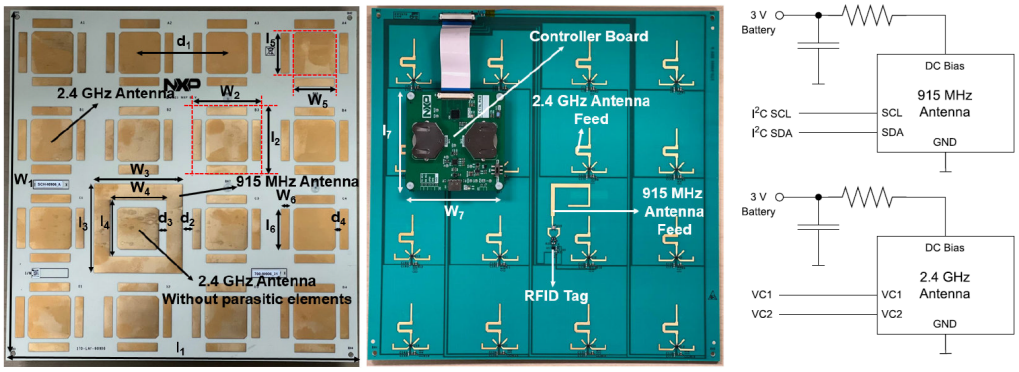

(a) (b) (c)

Fig. 2.10: An RIS unit from [27]. (a) Top view. (b) Bottom view. (c) Block diagram of the RFID antenna (higher) and a unit cell (lower).

the third layer is the ground plane with a feeding aperture for the patches and the fourth layer includes the feeding network with an RF switch, control and bias lines. The parasitic elements are there to create additional resonances and widen the impedance bandwidth of the unit cell. Unit cells have four different reflection phases controlled by the load impedance of the feeding network in the fourth layer. This load impedance is selected from four options by the RF switch. To integrate RFID communication, one of the unit cells has its parasitic elements replaced by a square ring antenna for the 915 MHz RFID signal. The authors produce multiple RIS units and use them to create a scaled up RIS aperture. They measured the radiation pattern of an 8×8 array (2 by 2 whole units) and found it to agree well with their simulated results. Lastly, a 16×16 array (4 by 4 whole units) was built and throughput measurements were performed for three scenarios. The three scenarios were indoor with no LOS, indoor with LOS and outdoor with no LOS. The RIS with its optimization algorithm consistently outperformed both the case where no RIS was present and where the RIS was present, but the reflection phases were random. In addition to the positive results, the RIS aperture together with the RFID control has low power consumption, only 0.336 mW.

The contributions mentioned above represent a selection of existing RIS designs. Each design offers a different approach and different interesting characteristics. Not all of these contributions had their design manufactured and experimentally validated.

As previously discussed, reconfigurable intelligent surfaces introduce the possibility of controlling the wireless communication environment in a meaningful way. [1] This fact changes the paradigm of wireless communications. This technology could enable new ways of improving communication protocols and even completely

new communication possibilities. [2] However before these appealing concepts can be fully realized, a foundational knowledge of how to appropriately model and design these systems must be created. There are three main points that need further investigation: RIS modeling, channel modeling for RIS-aided systems and RIS configuration optimization. [4] [2]

Firstly, the question of how to model the physical RIS needs to be discussed. [3] Existing models often ignore the mutual coupling of the cells, which is usually present since the cells are of sub-wavelength size. [2] Also reconfigurable intelligent surfaces are not able to provide reflection coefficients that all have an amplitude equal to 1 while simultaneously the phase can be set to any value. The amplitude and phase of the reflection coefficient are inherently linked and cannot be configured independently. [25] [2]

The second issue is channel modeling. Up until now, the channel was always regarded uncontrollable, but reconfigurable intelligent surfaces fundamentally change this by providing controllable paths. [1] Because of this, many of the existing models and formulae cannot be used, [4] for example, the well-known channel capacity formula introduced by Shannon. [3]

Lastly, better approaches to RIS configuration optimization need to be found. [2] Configuration optimization aims to find the optimal stimulus $\boldsymbol{\theta}$ (DC bias voltages of the varactor diodes) that configures the RIS with the most optimal reflection coefficients for the given scenario. The existing optimization methods are often either suboptimal or computationally very demanding and do not take into account the imperfect behavior of the given RIS. [2]

These points represent the main focus of RIS research. The RIS design proposed in this thesis aims to help achieve these research objectives by providing a prototype that can be easily used in many different tests and experiments. It is designed with scalability in mind and is easy to use. In the next part of this thesis the RIS prototype is introduced.

3 Scalable RIS prototype design

Reconfigurable intelligent surfaces present a research topic that changes the concept of wireless communication by introducing control over the wireless channel [1], [2]. Their properties are studied by multiple researchers and organizations all over the world, just as at the Institute of Telecommunications at the TU Wien in Vienna, Austria. The research efforts of the Institute of Telecommunications in regard to RIS prototypes and measurement validation started with the work of Zhao et al. [5], who designed a working prototype of an RIS, and Kerbler [28], who in his bachelor's thesis created a controller for the existing RIS prototype (see section 3.1). More recently a measurement setup dedicated to reconfigurable intelligent surfaces (see sub-section 3.5.1) was developed by Kiss et al. [6]. These efforts continue with the scalable RIS prototype introduced in this thesis.

The existing RIS module developed by Zhao et al. [5] experimentally demonstrated the working principle of RISs and serves as a proof of concept. For future research needs, an RIS module that is scalable and more focused on usability in testing setups is desired. The motivation of this thesis is to create an RIS module prototype that fulfills these requirements.

The rest of this chapter is organized as follows. In Section 3.1 the starting point of this thesis is presented, the RIS design of Zhao et al. [5] and RIS controller by Kerbler [28]. Afterwards sections 3.2, 3.3 and 3.4 describe the design process of the proposed scalable RIS module. The measurement results of the RIS prototype together with an introduction to the measurement setup used are featured in Section 3.5. Lastly, in Section 3.5.3, the measurement results, the positive aspects of the RIS prototype, and the research outlook are discussed.

3.1 Prior work

In this section, the starting point of this thesis is presented. The existing RIS module and the associated RIS controller are introduced.

The existing RIS module was developed by Zhao et al. [5]. It is an RIS controlled by reverse-biased varactor diodes. It is designed to operate at a frequency of 5 GHz. Unit cells (see figure 3.1) are square and consist of a square patch with side length $a = 13$ mm and a square ring with inner and outer side lengths $b = 14$ mm and $c = 15$ mm interconnected by four varactor diodes on the top layer and a ground plane on the bottom layer. Two slots with width $g = 0.1$ mm that are perpendicular to each other are cut into the patch and ring and resemble the letter "X". The substrate used has thickness $t = 1.524$ mm and is made of Rogers RO4003C with relative permittivity $\varepsilon_r = 3.55$ [−].

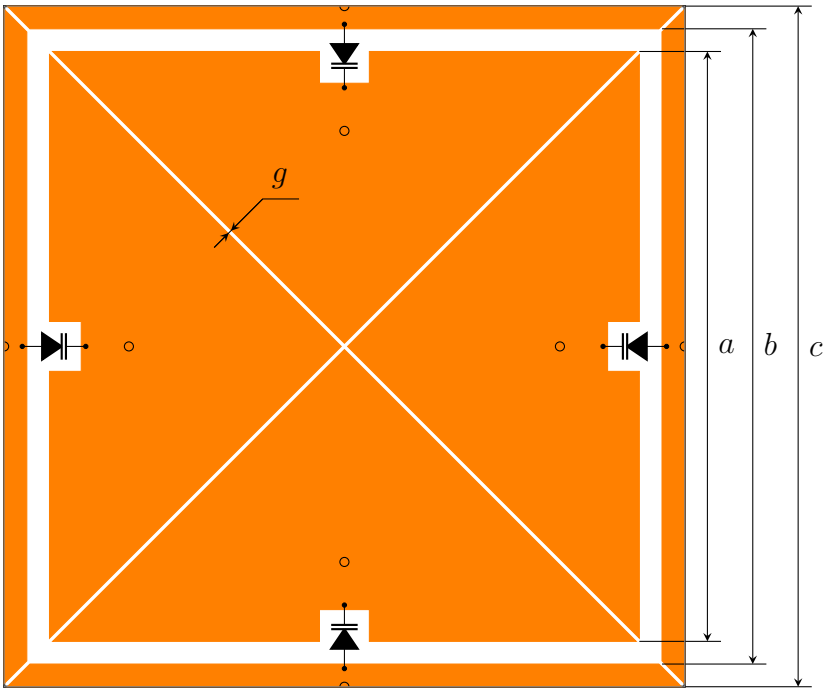

Fig. 3.1: RIS Unit Cell by Zhao et al. [5].

The manufactured prototype (see figure 3.2) consists of a 6×6 array of unit cells and a connector. The RIS array has dimensions 90 mm $\times$ 90 mm and is surrounded by a border (the red part in figure 3.2). Unit cells are divided into nine groups of four unit cells each (2×2 array). The bias voltages can be set independently for each cell group. All cells in one group have the same bias voltage.

The RIS module was then tested. The measurement setup consisted of the RIS module biased evenly by a power supply (all groups had the same bias voltage). Two horn antennas connected to a R&S ZVA8 *vector network analyzer* (VNA) served as transmitter and receiver. The transmitter (port 1 of the VNA) was positioned so that the emitted wave hits the RIS perpendicularly ($\theta_i = 0°$). The receiver (VNA port 2) was located at angle $\theta_r = 45°$.

The transmission S_{21} of the RIS channel was measured at frequencies from 4.9 GHz to 5.1 GHz for 8 different bias voltages: 0 V, 4.2 V, 5.3 V, 6 V, 6.6 V, 7.6 V, 9.5 V and 21 V. The measurement results show that the manufactured module was able to introduce variable phase shifts with good agreement between the simulations and the measurement results. The measured results compared to the simulations are depicted in figure 3.3. For more details see the original text of Zhao et al. [5].

The RIS controller was the result of the bachelor's thesis of M. Kerbler [28]. The RIS controller provides the bias voltages for the RIS module. The controller can be remote-controlled by a computer. The RIS controller consists of a *micro-controller unit* (MCU) that can communicate with a computer and a *digital-to-*

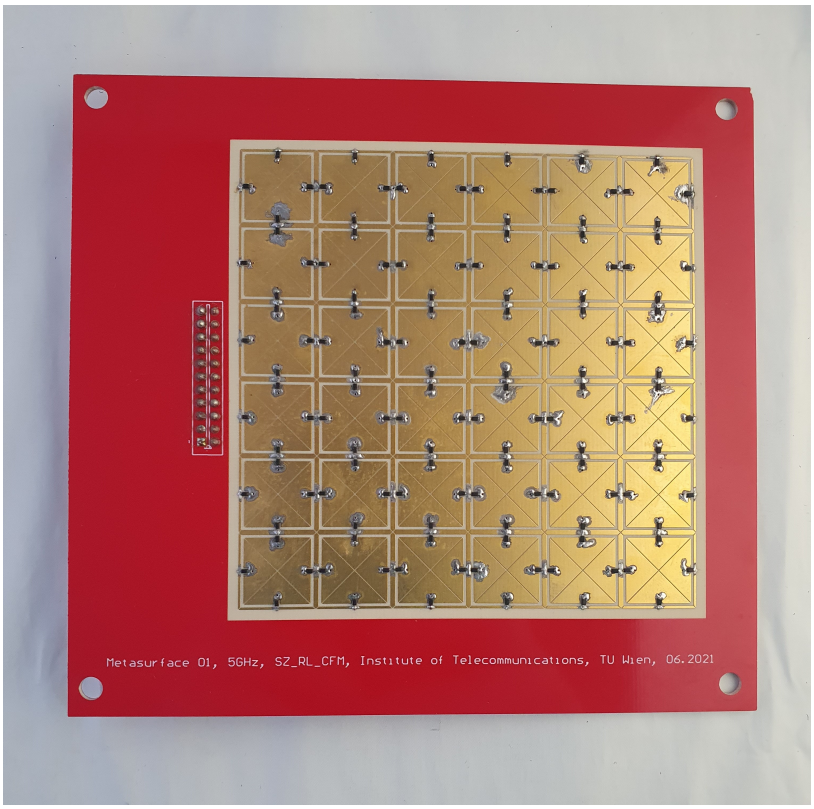

Fig. 3.2: The manufactured RIS module by Zhao et al. [5].

analog converter (DAC) that the microcontroller controls. The MCU unit used is the evaluation module "MSP430FR5969 Launch Pad" and the DAC is the evaluation module "DAC81416EVM" both by Texas Instruments. The MCU communicates with the computer via USB and with the DAC via *serial peripheral interface* (SPI). The DAC has 16 analog outputs and can theoretically provide voltages of up to 40 V. However, in his work Kerbler found that due to a failure of the DAC-board voltages higher than 10 V could not be used – supplying the board with higher voltages led to permanent damage to the DAC chip.

3.2 Necessary changes to the RIS module design

The starting point for this thesis was established in the previous section. As mentioned above, the goal of this work is to create a scalable RIS prototype. However, the requirement of scalability dictates multiple changes to the design. An overview of these necessary changes together with the reasons for them is given in this section.

The scalable nature of the RIS module prototype refers to the possibility of mounting multiple modules side-by-side, creating a larger RIS. Unit cells in this

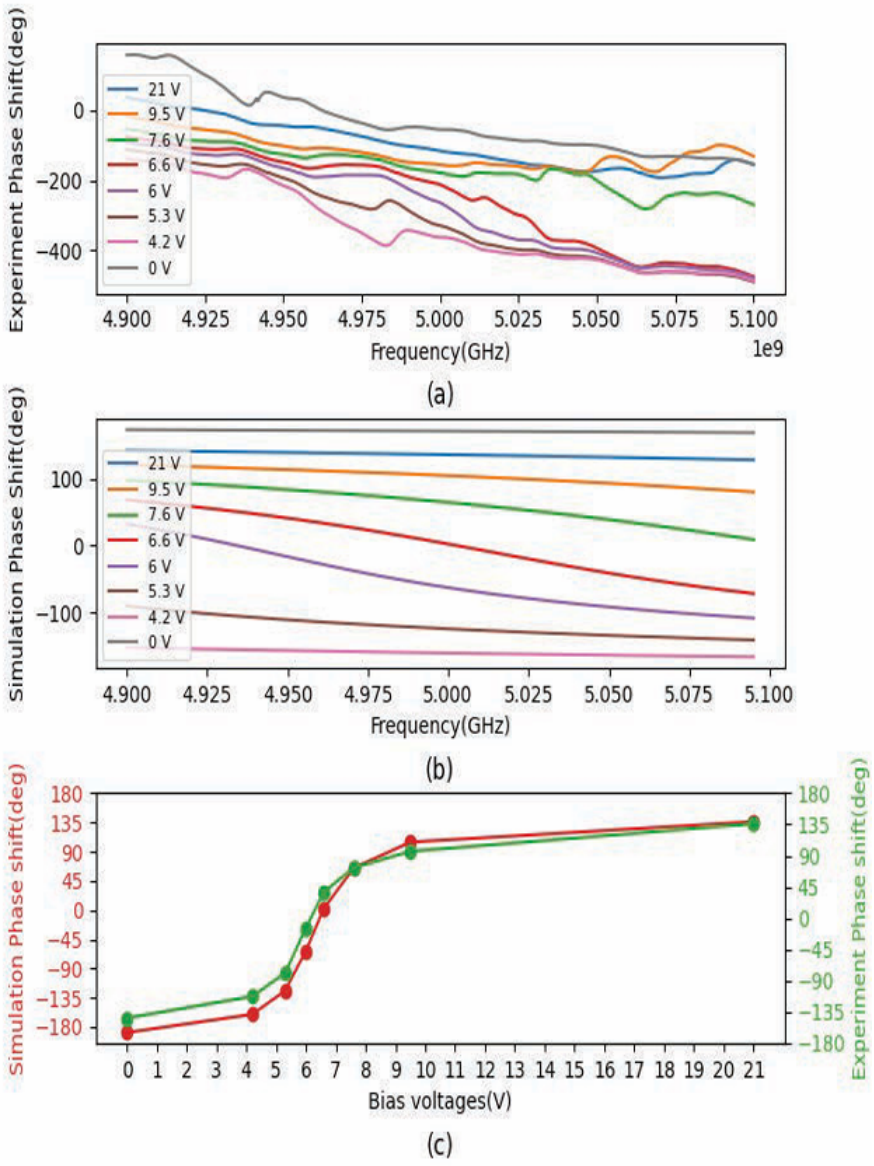

Fig. 3.3: Phase of the transmission coefficients S_{21} in the frequency band 4.9 GHz to 5.1 GHz for eight bias voltages of the RIS: a) measured values, b) simulated values and c) simulated vs. measured phases at operating frequency 5 GHz. Taken from [5].

up-scaled RIS should still retain a periodic structure with no unnecessary gaps. If the RIS modules had borders, as seen in Figure 3.2, then there would be large gaps between some unit cells. In this case, the up-scaled RIS is not a periodic array of unit cells, which is not desired. Therefore, the RIS module *printed circuit board* (PCB) can not have any borders.

The main lumped electronic components used in the RIS module design are

varactor diodes. The varactor diodes are essential for the unit cell design and are, of course, part of the unit cells. However, other components are needed for a fully functional RIS module, e. g. a connector to the RIS controller. These auxiliary components are not meant to be part of the active part, the unit cells; therefore, they need to be placed away from the unit cells. Since there is not going to be a border on the proposed PCB, these components must be placed on the backside of the RIS module. For more information on the components used, see sections 3.3 and 3.4.

Every RIS module also needs a biasing network that provides a connection between the varactor diodes and the DAC of the RIS controller. This biasing network was previously routed inside the ground plane of the unit cells. For the proposed module design, the routing network is in a separate PCB layer. This means that the RIS module PCB needs to have at least 4 layers. Then the ground plane of the unit cells remains intact and the RIS behavior can be simulated more precisely.

For the same reason, all components need to be *surface-mounted devices* (SMDs). If through-hole components were used, the ground plane and even the top layer with the patches would be damaged.

In summary, to create a scalable RIS module, these changes are going to be implemented:

- the design is borderless;
- auxiliary components are mounted on the backside;
- components are SMD;
- and the PCB has 4 layers.

3.3 Unit cell redesign and simulation

This section deals with the design of unit cells with regard to the high-frequency behavior of the RIS module. Differences in the high-frequency behavior of the RIS introduced by the design changes mentioned above are observed and, when necessary, compensated for. Ansys HFSS is used to simulate the RIS behavior.

The RIS unit cell of Zhao et al. [5] was recreated in Ansys HFSS. The simulation setup uses a floquet port and coupled boundaries to simulate an infinitely large periodic planar array of unit cells: an infinitely large RIS. For the sake of simplicity, the only cutouts in the ground plane of the unit cell in this two-layer model are around the patch vias that connect to the bias voltages. Cutouts and gaps that would result from the biasing network are not simulated (see Fig. 3.12 for a view of the biasing network). A screenshot of the unit cell in HFSS can be seen in figure 3.4.

For convenience and better comparison between the existing unit cell design and the proposed design, the same bias voltages U_{bias} are used. These eight voltages span

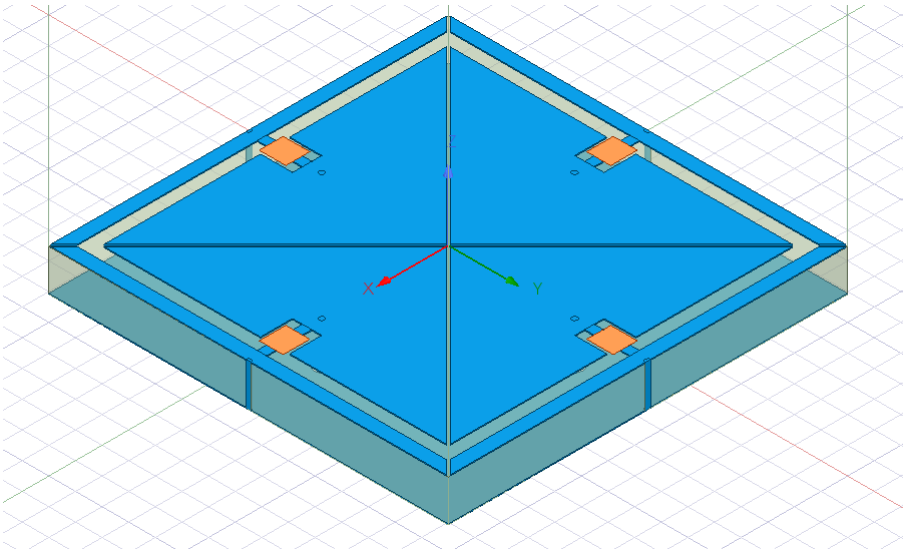

Fig. 3.4: View of the RIS unit cell with two-layer model in the simulation tool Ansys HFSS.

the entire bias voltage range of the varactor diodes (SMV2019-079LF by Skyworks). The varactor diodes are simulated as their equivalent passive circuits at the given voltage.

The biggest design alteration to the RIS design is the switch to a 4-layer stackup. Conventional multilayer PCBs have substrate thicknesses in the range of tenths of millimeters. The substrate of the RIS has a thickness much greater in comparison. Having a lower substrate thickness would make the PCB better suited to existing manufacturing processes and reduce cost.

The effects of decreasing the substrate thickness on the behavior of the RIS are investigated. The starting point, the original value $t = 1.524$ mm, was decreased in increments of 0.1 mm down to $t = 1.024$ mm. The phase responses of four chosen thicknesses are shown in figure 3.5.

Phase responses move up in frequency with decreasing substrate thickness t. The phase transition from 180° to −180° also becomes progressively more steep, corresponding to a decrease in the bandwidth of the resonances. This does not seem to hold for $U_{bias} = 0$ V. In addition, for some bias voltages, the phase behavior of the resonance changed completely. This is best seen for $U_{bias} = 4.2$ V. When $t = 1.324$ mm, the phase transition features a discontinuous step while for the next lower thickness $t = 1.224$ mm, the phase does not transition to −180° after the resonance but returns to 180°. The same change can be seen for $U_{bias} = 5.3$ V and even the phase response of $U_{bias} = 6$ V has a discontinuity at $t = 1.024$ mm.

The changes in the magnitude response correspond to the changes in the phase

response. With decreasing substrate thickness, the magnitude responses move to higher frequencies, their bandwidth decreases, and their minima are lower, indicating a higher quality factor.

For the proposed RIS, these effects are undesirable. The higher steepness of the phase transition limits the usable bias voltage range, which puts increased demand on bias precision and RIS manufacturing. The change in the resonant phase behavior further limits the usable bias voltages. This leads to the conclusion that for the proposed RIS the substrate thickness will not change. However, for a RIS design that focuses on 1-bit encoding (two discrete phase states), a decrease in substrate thickness is worth exploring.

Since the thickness of the Rogers substrate remains the same, the complete 4-layer stackup can be added to the simulation model. The stackup is chosen to be symmetrical to prevent bow and twist of the PCB in the manufacturing process. For this reason, an FR4 prepreg layer with thickness $t_{pp} = 0.356$ mm and a FR4 bottom core layer with the same thickness as the *high frequency* (HF) Rogers substrate $t_{bottom} = t = 1.5$ mm are added to the simulation. Table 3.1 depicts the simulated stackup. The vias in the patches have adjusted height so they reach onto the Bottom Layer.

No.	Name	Material	Thickness [mm]	ε_r [-]
1	Top Layer	copper	0.035	-
2	HF Substrate	RO4003C	1.524	3.55
3	Ground Plane	copper	0.035	-
4	Prepreg	FR4	0.356	4.8
5	Layer 3	copper	0.035	-
6	Bottom Substrate	FR4	1.5	4.8
7	Bottom Layer	copper	0.035	-

Table 3.1: RIS PCB four-layer stackup used in simulations (is the same as the manufactured stackup). The 'Top Layer', 'HF Substrate' and 'Ground Plane' layers constitute the active part of the unit cells.

In Figure 3.6, we can see the phase and magnitude responses for the two- and four-layer models. For nearly all bias voltages, the differences between the two- and four-layer models are minimal. Slight frequency shifts and small magnitude differences. The greatest change occurs at bias voltage 4.2 V. We can see a frequency shift of the primary resonance by 350 MHz to lower frequencies and the magnitude minimum changed. For the primary resonance now at 4.35 GHz, the minimum is higher by 4.3 dB.

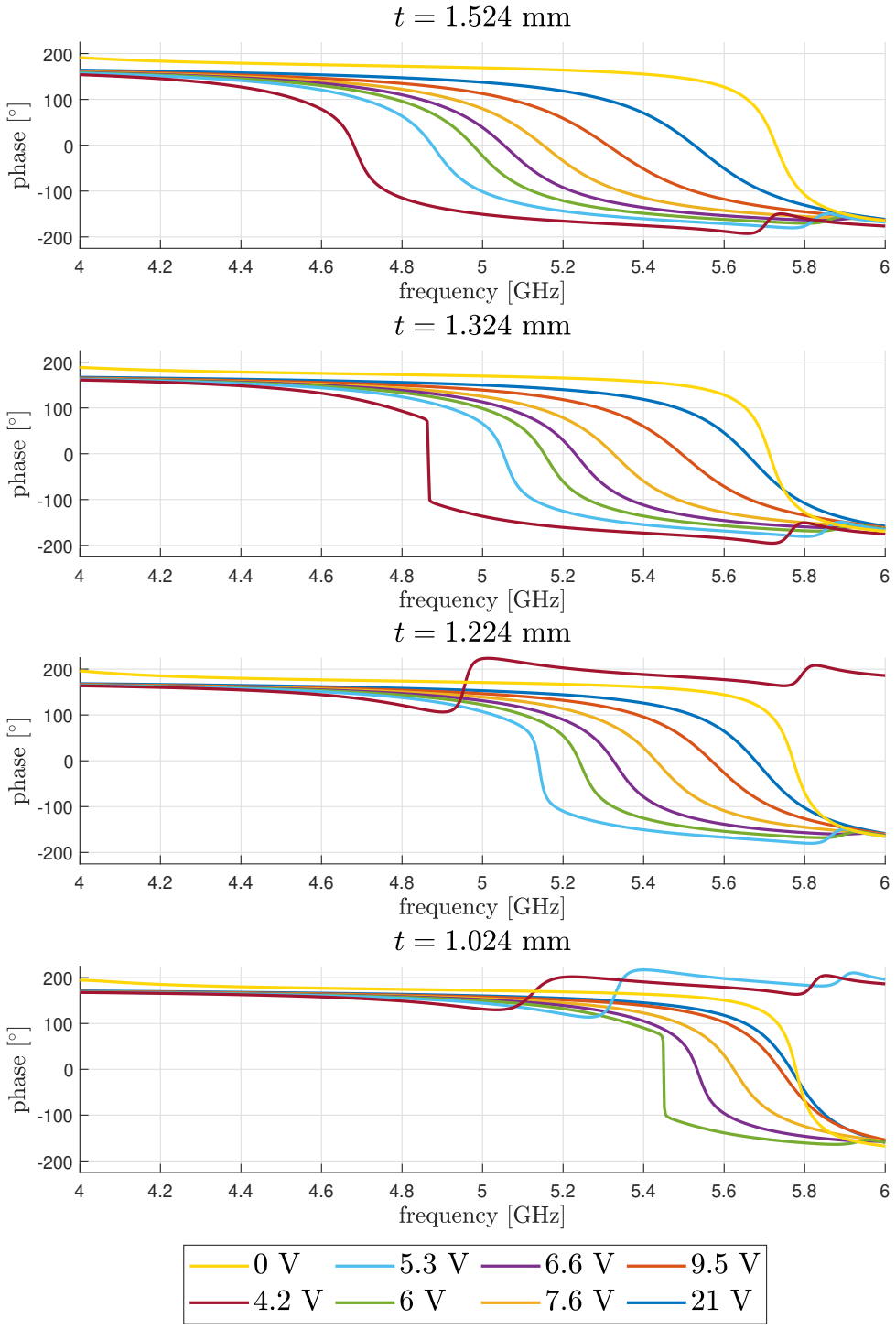

Fig. 3.5: Phase responses of the simulated RIS structure for four different thicknesses at the chosen bias voltages U_{bias}.

There are secondary resonances present for every bias voltage at around 5.6 GHz. These get more pronounced in the four-layer model: lower magnitude minima and

more pronounced phase changes. For bias voltage 4.2 V the secondary resonance shifts down by 160 MHz, similarly to the primary resonance at this bias voltage.

Although the above-mentioned changes are present, the tunable phase range at operational frequency 5 GHz does not change much. The phase response at 5 GHz only changes by 5° to 10° except for $U_{bias} = 5.3$ V, where it changes by 17°, and, of course, for $U_{bias} = 4.2$ V, where it changes by 28°. However, the end points of the tunable phase are given by the minimum and maximum bias voltages, $U_{bias} = 0$ V and $U_{bias} = 21$ V, respectively. This means that the tunable phase range remains nearly identical, increasing only 5°. This best seen when the reflection coefficient is displayed in the complex plane when varying the bias voltage (see Figure 3.7). The bigger phase changes at bias voltages 4.2 V and 5.3 V only mean that the phase is more sensitive to the bias voltage at these values. It is also important to note that the two-layer model does not take into account gaps and cutouts caused by the biasing network, the comparison is skewed in favor of the two-layer model.

The footprint of the varactor diodes recommended by the manufacturer was added to the unit cell to improve the soldering process. The cutouts in the patches have been altered to accommodate the footprint. The addition of the footprint had some influence on the reflection behavior of the RIS. Magnitude minima got lower for the primary resonances and more so for the secondary resonances. Moreover, slightly increased phase steepness of the primary resonances and slight frequency shifts can be observed.

Additional changes have been made to the design based on the manufacturers capabilities and requirements. These changes overall lead to the primary resonances being shifted up in frequency and become steeper. To compensate for these effects, the horizontal dimensions of the unit cell were altered. The final dimensions of the unit cell together with the simulated reflection behavior are introduced below.

3.3.1 Proposed RIS unit cell design

Figure 3.8 shows the final layout of the unit cells. The unit cells are square and consist of a square patch surrounded by a ring. The side length of the patch is $a = 13.5$ mm and the ring has an inner side length $b = 14.5$ mm and an outer side length $c = 15.5$ mm. The patch and ring are divided into four pieces each by two slots on the diagonals of the unit cell, resembling the letter "X". The width of these slots is $g = 0.106$ mm. The patch and ring segments are connected by four varactor diodes (SMV2019-079LF by Skyworks). There are cutouts in the patch segments so that the recommended footprint of the varactor diodes can be accommodated. The cutouts have a width of 1.1 mm and a depth of 1.2 mm. The pads of the diode footprint are square with side length 0.35 mm. The diodes are

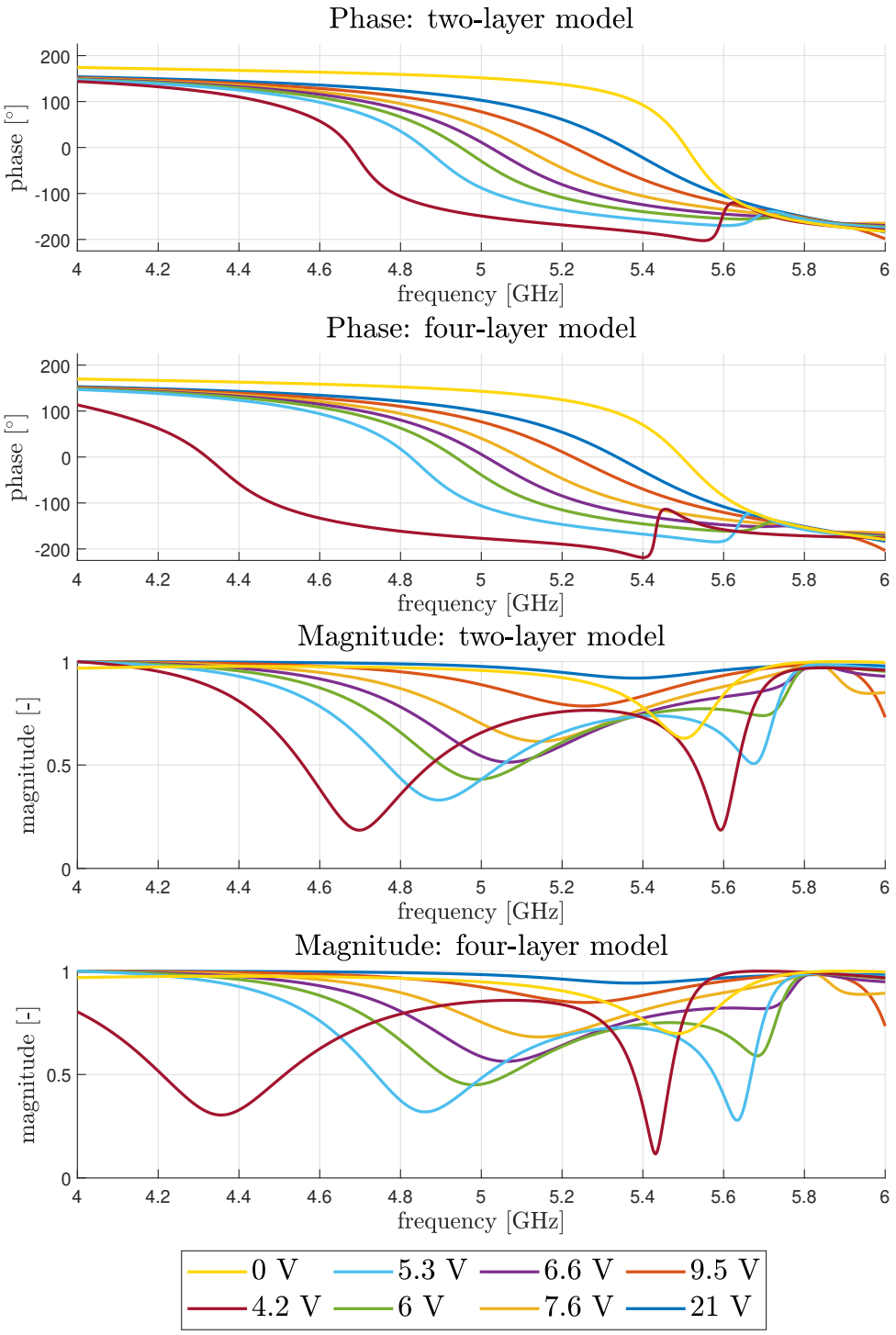

Fig. 3.6: Phase and magnitude responses for the two- and four-layer model at eight different bias voltages U_{bias}. The upper two graphs show the phase responses while the lower two show the magnitude responses.

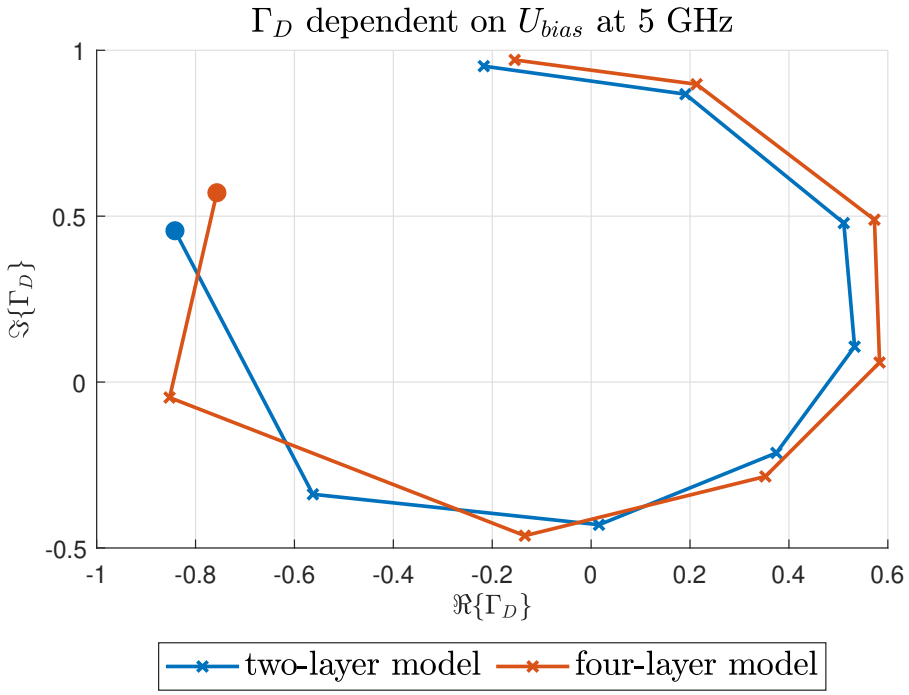

Fig. 3.7: Reflection coefficients Γ_D at 5 GHz for the two- and four-layer model for the chosen bias voltages U_{bias}. Represented in the complex plane. The value for $U_{bias} = 0$ V is represented by a point in the respective color.

placed so that their cathodes are connected to the patch and anodes to the ring: reverse polarization. Vias connect the ring to the ground plane and the patch to a bias voltage U_{bias} (more details below). Ring segments of neighboring cells that are connected together always share one via that is placed in the middle. Vias connecting the patch segments to the biasing network are located 4.25 mm from the center of the unit cell. The unit cell substrate is made of Rogers RO4003C material with relative permittivity $\varepsilon_r = 3.55$ and thickness $t = 1.524$ mm. On the bottom of this substrate there is the ground plane of the unit cells. The ground plane is continuous, except for cutouts around the patch vias. Below the ground plane are the remaining layers of the four-layer design of the RIS. The complete stackup is listed in Table 3.1.

The simulated phase and magnitude responses of the proposed RIS unit cell design are shown in Figure 3.9. In the phase response, we can see that by changing the bias voltage U_{bias} the phase of the reflection of the RIS can be controlled. This is given by the changing capacitance of the reverse-polarized varactor diodes. The primary resonance of the RIS dictates the steepness and frequency of the phase

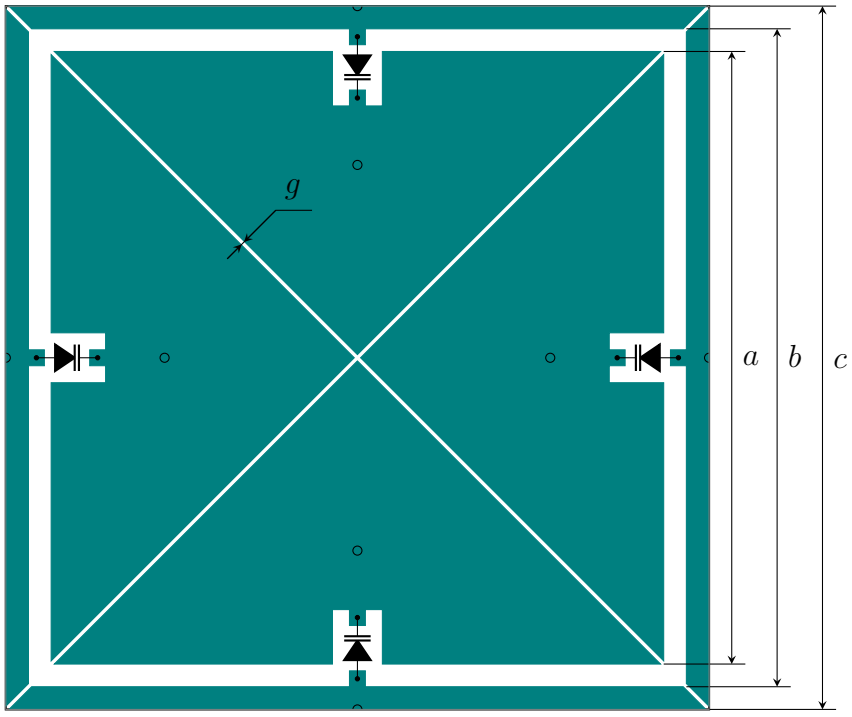

Fig. 3.8: proposed RIS Unit Cell.

transition from 180° to 180°. The phase response in 3.9 shows that at the operation frequency 5 GHz the achievable reflection phases are spaced throughout the bias voltage range. The tunable phase range spans 316°. The relation between the simulated reflection phase and the bias voltage applied at 5 GHz is depicted in the tuning diagram in Figure 3.10. Note that while in Figure 3.9 the phase for $U_{bias} = 0$ V at 5 GHz is 143°, in the tuning diagram in Figure 3.10 it is -217°. These values are equivalent for these purposes, since their difference is one full rotation 360°. Therefore, for the tuning diagram, the unwrapped phase value of -217° was chosen to better show the tuning effect. This difference was also touched on earlier, and the complex plane representation of the reflection coefficients depicted in Figure 3.7 gives even more context (Figure 3.7 is mentioned for illustration).

3.4 Bias network, mounting and other considerations

After the unit cell design and the PCB stackup were chosen, all other design choices had to be made. In this section, the RIS modules (one RIS PCB) are discussed. The amount of unit cells per module, biasing groups, routing, mounting, and other design considerations are explored.

Figures 3.11, 3.12 show the front and back of an assembled RIS module respectively. The module has a 6×6 array of unit cells. As mentioned above in Section

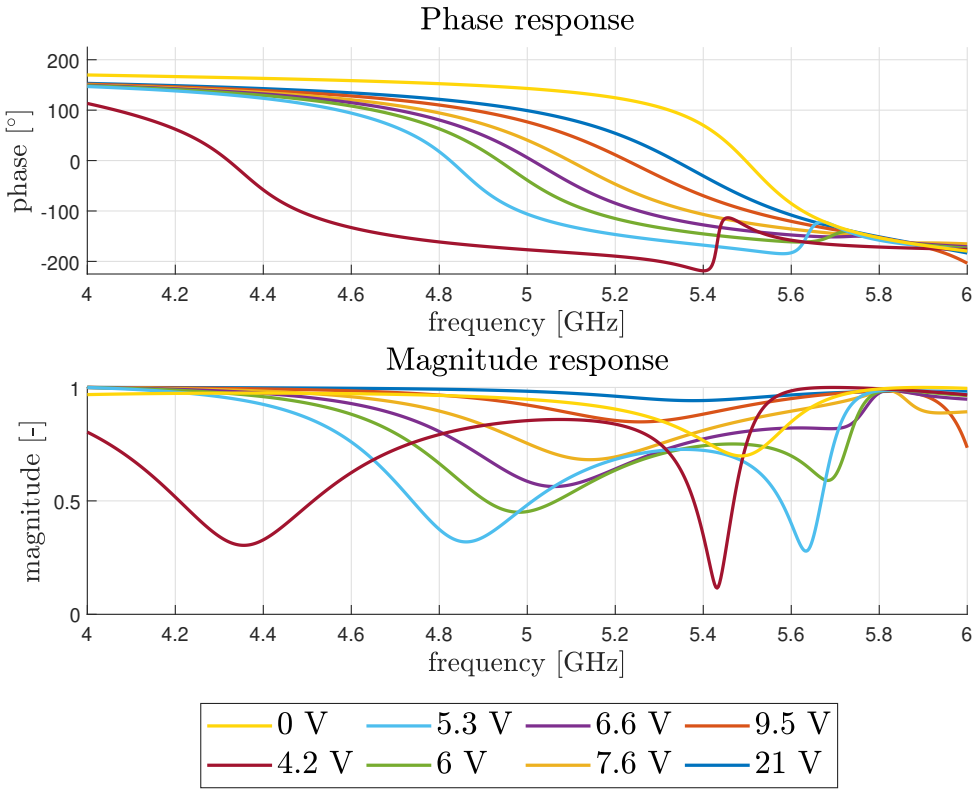

Fig. 3.9: Phase and magnitude responses of the final unit cell design depicted in Fig. 3.8 for eight chosen bias voltages U_{bias}.

3.2, the RIS module should ideally not have borders. However, manufacturing limitations did not allow for that, thus a minimal border of 0.5 mm was added. The finished PCB size of the module is 94 mm × 94 mm, where the unit cells make up $6 \cdot 15.5$ mm = 93 mm and the added border $2 \cdot 0.5$ mm = 1 mm. Each unit cell has four varactor diodes (SMV2019-079LF), making it 144 diodes in total for one module. On the back of the module, there are 10 pin connectors and 4 mounting connectors.

The unit cells are divided into nine groups of 2×2 cells. All groups and cells are assigned numbers. The numbering system is visualized in Figure 3.13. The groups are numbered `I` to `IX` starting from the lower left corner to the upper right corner row by row when looking at the front of the module. The unit cells in each group are further numbered from `1` to `4` in the same manner. Therefore, the unit cell that is fifth from the left and third from the bottom would be numbered: group `VI`, cell `1`, for example. The group and cell numbers are printed on the back of the respective group or unit cell (see Figure 3.12).

The bias network is routed in two stages. First, the diodes inside one cell group are routed to their respective group connector `I-IX`, and secondly, the group con-

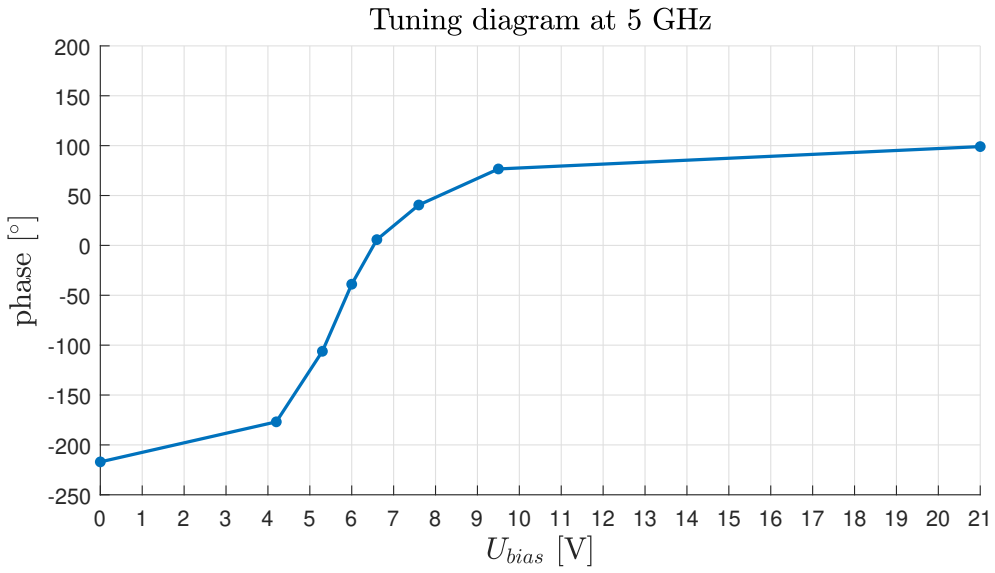

Fig. 3.10: Tuning diagram (the dependence of the reflection phase on the bias voltage applied) of the proposed unit cell design at operation frequency 5 GHz.

nectors are routed to the central RIS module connector `J1`. The complete schematic of the RIS module is shown in Appendix A.

The diodes in one cell are always connected in parallel, their anodes are connected to ground, and their cathodes are connected to one pin of the group connector. This ensures reverse biasing of the diodes. The group connector is located on the back of the module in the middle of the cell group (see Figure 3.12). Cell `1` diodes are connected to pin 7, cell `2` to pin 5, cell `3` to pin 9 and cell `4` diodes to pin 3 of the respective group connector. Pins `4`, `6`, `8` and `10` are connected and then routed to the module connector `J1`. The pin connections of the group connectors are shown in Figure 3.14 on the left. When the RIS module is used in its default mode (9 controllable groups as shown in Figure 3.13) the counterpart of the group connector acts as an array of jumpers; the pins opposite each other are connected as they would with a jumper. Pin `1` → pin `2`, pin `3` → pin `4`, pin `5` → pin `6` and so on. In this way, all the cells in a group are connected to one module connector pin, ergo one bias voltage. How these "jumpers" look is shown in Figure 3.16.

In the future, these group connectors can be used to create controllable groups of any shape and granularity. For example, one could have each column as a group, or even each unit cell can be controlled separately. The only requirement is to make the appropriate connection to the DAC, or DACs used. Otherwise, there are no limitations as to how the unit cells can be divided into groups. In these cases, the module connector `J1` would not be used.

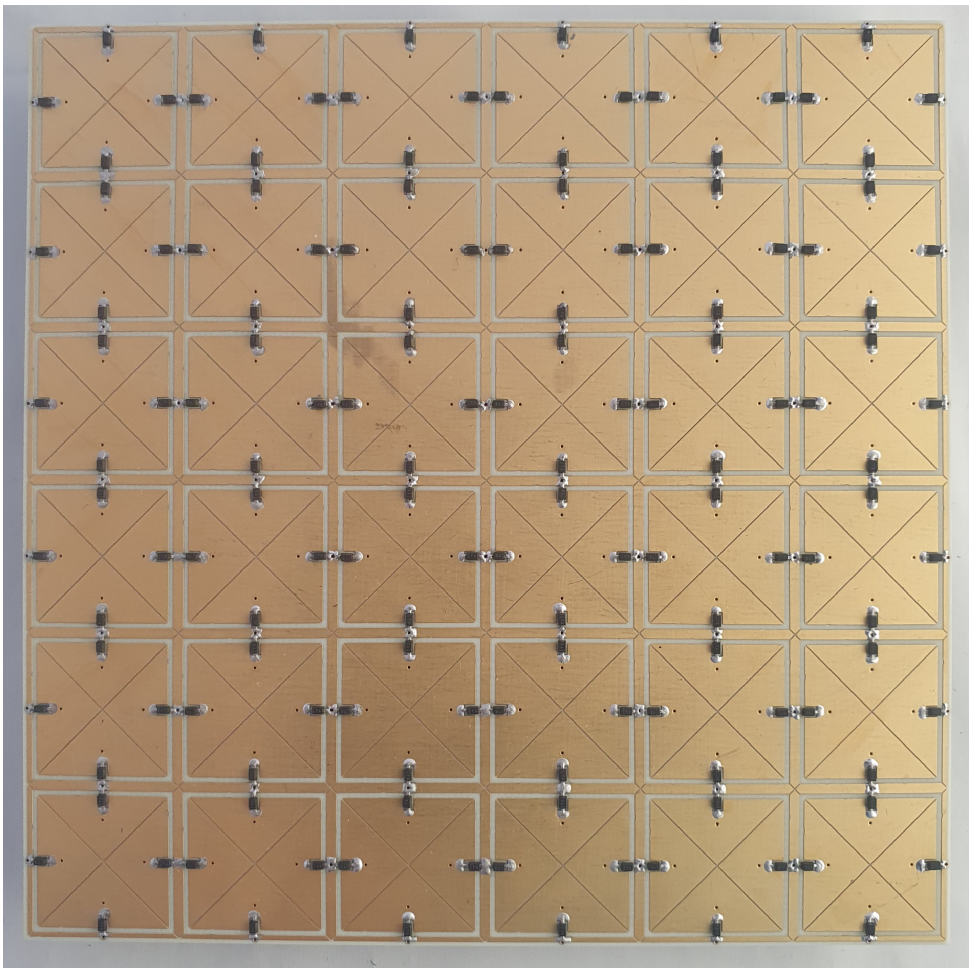

Fig. 3.11: Photo of the front side of an assembled RIS module: the unit cells; 6×6 unit cells with four varactor diodes each for a total of 144 varactor diodes.

The module connector `J1` serves as an interface to connect a DAC to the RIS module. It is located between the group connectors `V` and `VIII`. The module connector distributes the biasing voltages U_{bias} sourced from the DAC to the cell groups. The pin assignment of this connector is shown in Figure 3.14 on the right. As mentioned earlier, when a non-default cell grouping is desired, this connector is not in use. In that case, the bias voltage routes should be connected to ground either on the module connector side or the group connector side.

The connectors used have a pitch of 1.27 mm or 0.050 inches. This pitch was chosen because a larger pitch would lead to problems in placing the connectors on the PCB. The unconventional stackup used meant that all vias had to be through-hole, connecting through the entire PCB. This fact caused the space problems mentioned above. The pin amount of the connectors was chosen so that each signal cable (U_{bias}) has its own ground cable, thus minimizing the induced interference on the cables.

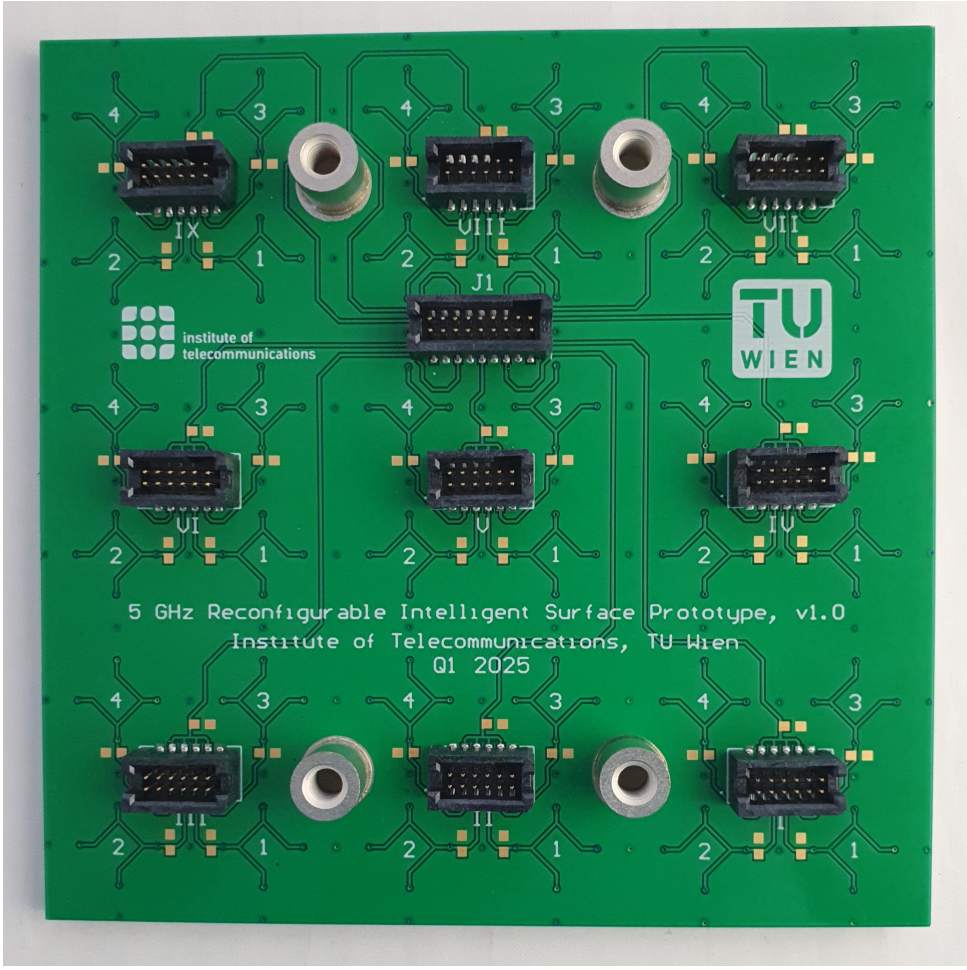

Fig. 3.12: Photo of the back side of an assembled RIS module; the routing network for the unit cell groups and module mounting. One main connector to control the 9 groups (`J1`), 9 connectors (`I` to `IX`) that serve as an interface for each group (these enable the control of each unit cell individually in the future). Four mounting connectors with internal M4 threads.

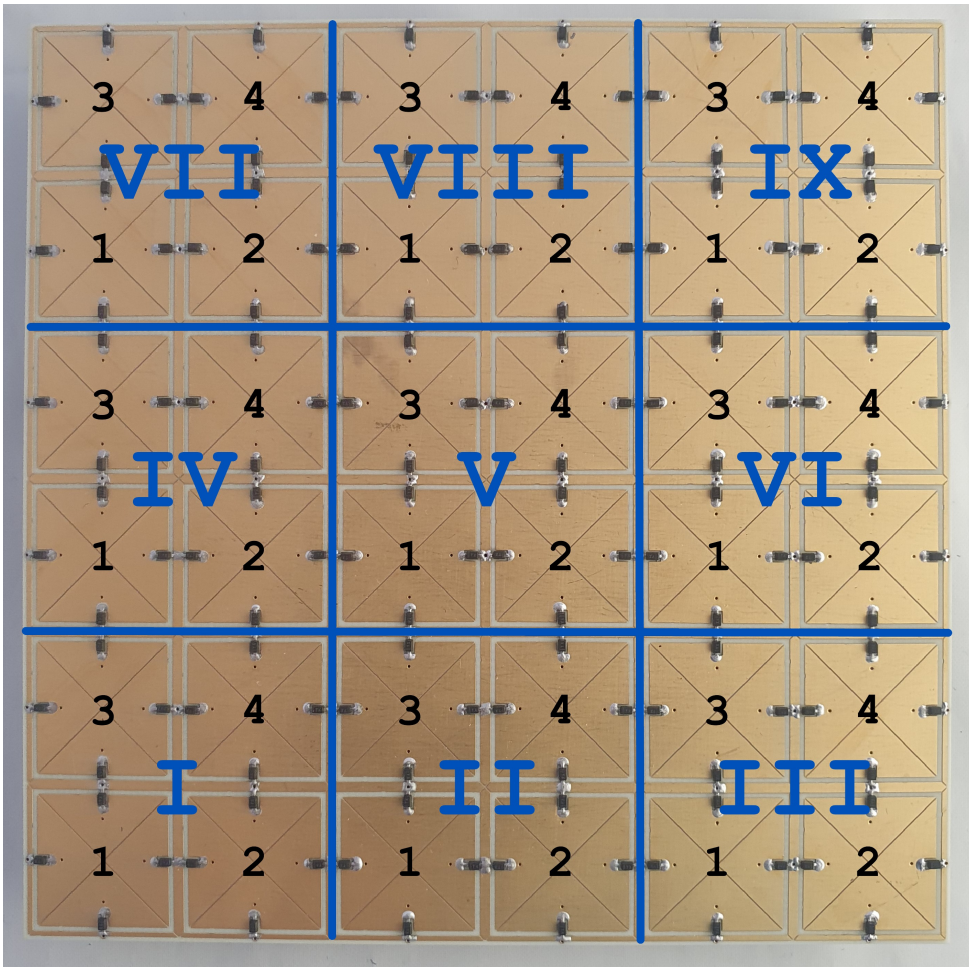

Fig. 3.13: Numbering of unit cells visualized on the front of the RIS module. The module is divided into nine groups of 2×2 unit cells, numbered `I` through `IX`. Each group has its four unit cells numbered `1` through `4`. Therefore, the unit cell that is fifth from the left and third from the bottom would be numbered: group VI, cell 1, for example. The numbering is printed on the back of the RIS module (see Fig. 3.12).

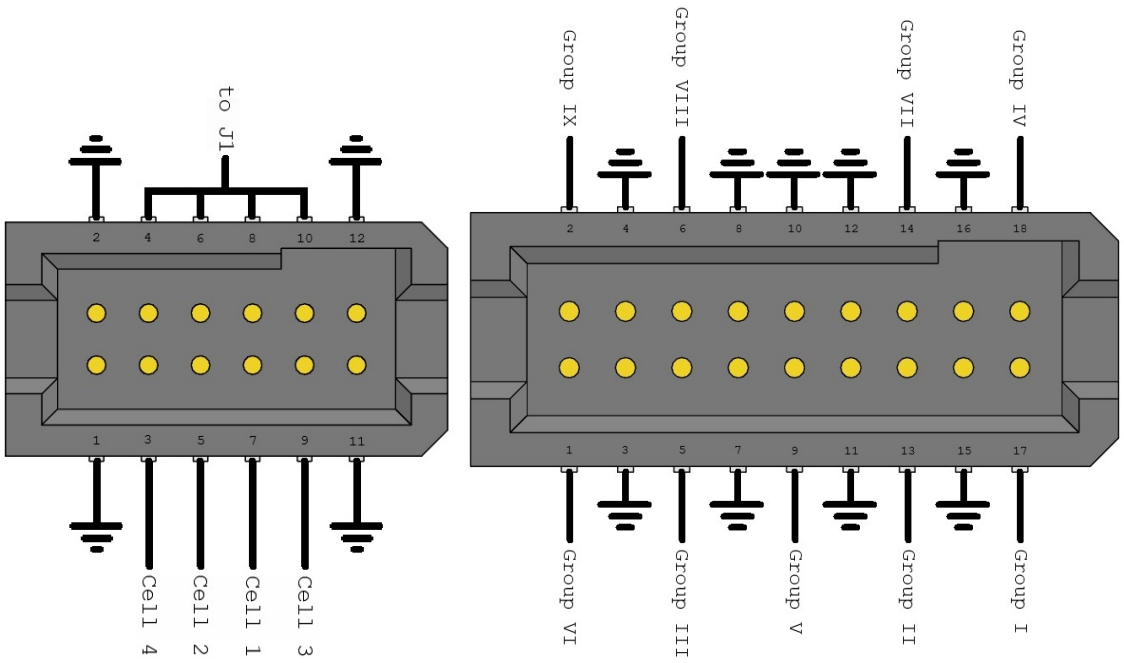

Fig. 3.14: Pin assignments of the two connector types on the RIS module. On the left there is one of the group connectors (`I-IX`) and on the right there is the module connector `J1`.

For the RIS module, the standard mounting method of using screws and holes in the PCB could not be used. The easiest solution to mount the RIS module found was to use cylinder SMD components that have an internal blind-hole thread (see Fig. 3.12). The size of the thread is M4. These four components are used as mounting adapters. Commonly available spacers can then be used to mount the RIS module to where ever needed.

With this mounting method, one or more RIS modules can be easily installed on appropriate adapter plates. In this way, the RIS design achieves scalability. Some examples of possible RIS configurations are shown in Figure 3.15. The possible upscaled RISs are not limited to planar configurations; 90° and rounded corner RISs can be created. Figure 3.16 shows how two RIS modules are mounted in a 1×2 configuration in the measurement process.

The chosen surface finish of the RIS module PCBs is *direct immersion gold* (DIG). Direct immersion gold was chosen because it does not contain nickel. Surface finishes with nickel, like *electroless nickel immersion gold* (ENIG) and *electroless nickel electroless palladium immersion gold* (ENEPIG), cause noticeable loss in reflected waves. To avoid this, the less common DIG surface finish was chosen for the RIS modules.

In this section, the bias network and mounting of the RIS modules were de-

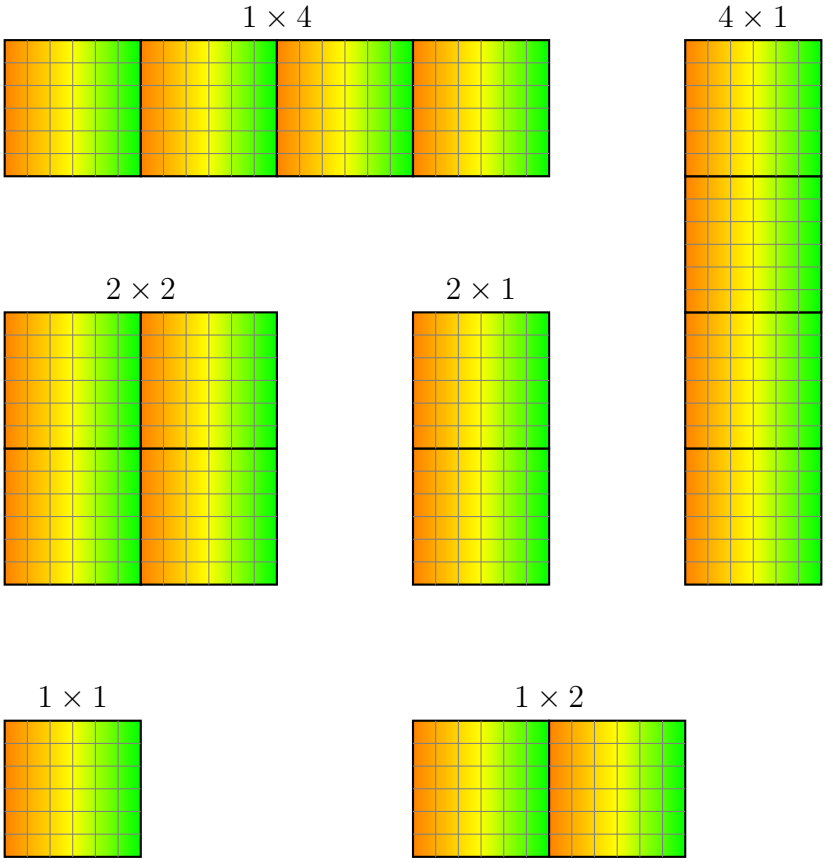

Fig. 3.15: Several possible configurations of RIS modules to achieve various shapes and sizes: scalability.

scribed. Due to the design of the bias network, the RIS module can be freely divided into controllable groups; Column, row, and cell control is possible. The default grouping is nine square groups of four unit cells (2×2 cells). The RIS module can be mounted to any suitable surface thanks to the mounting adapters. The mounting adapters are cylinder-shaped SMD components with an internal M4 thread. In this way, RIS can be easily scaled up by mounting multiple modules. For measurements, spacers and adapter plates were used to attach the RIS modules to the testbed. The surface finish is nickel-free to prevent unnecessary loss of reflected waves and there is an option to add HF shorting capacitors to each cell and group, if necessary.

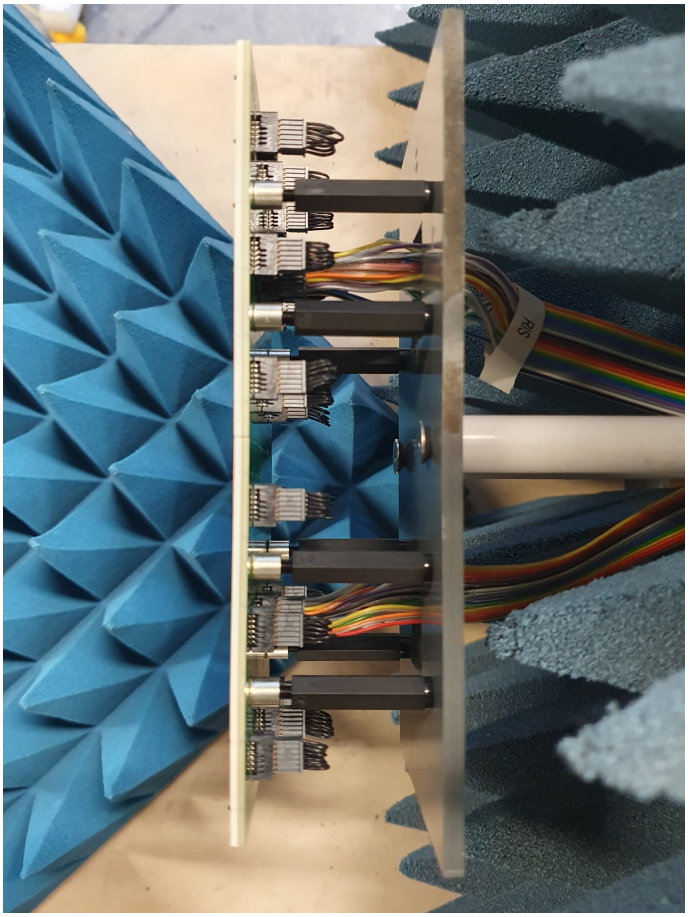

Fig. 3.16: Top view of and up-scaled RIS consisting of two modules in a 1×2 configuration. The modules are on the left. Spacers are used to connect the mounting adapters of the RIS modules to the adapter plate (dark gray, on the right). The adapter plate also has two holes to connect to the testbed (light gray rods on the right) and two holes for the RIS-to-DAC cable connection. The "jumpers" used for the group connectors are also visible.

3.5 Measurements of the RIS prototype

The following section describes the measurements of one RIS module and an up-scaled RIS consisting of two modules in a 1×2 configuration. First, the measurement testbed is introduced and later the measurements of a single module and the up-scaled RIS are presented.

3.5.1 Measurement setup

Figure 3.17 shows the measurement setup. This setup was first implemented by Kiss et al. [6].

The measurement is performed by the vector network analyzer ZVA 24 by Rohde & Schwarz. Two horn antennas are connected to ports 1 and 2 of the VNA. The two antennas are used to illuminate the RIS and receive the reflected portion of the signal. The antennas are placed on a 3 m long linear spindle drive and can be rotated by rotation units. Special coaxial cables that provide stable amplitude and phase properties when moved are used to connect the antennas to the VNA.

The stand for the tested RIS is placed on another spindle drive (length 0.76 m) that is perpendicular to the center of the antenna spindle drive. The RIS is connected to the stand by its own adapter plate (as shown in Fig. 3.16) and two rods. There is a back plate with absorbers (dark blue) mounted on the stand. More absorbers are placed in front of the RIS stand (light blue) and behind the stand on wooden racks (dark gray).

Currently, multiple DACs can be used for RIS biasing. The RIS controller from [28] was revised by the author of [29]. A newer version of the DAC evaluation model, "DAC81416EVM08", is used as the primary DAC. The newer evaluation board has an FTDI microchip designated for communication over *universal serial bus* (USB). Therefore, there is no need for the MCU used previously. The new DAC evaluation module handles communication and controls other DACs through daisy chaining. The functionality of the daisy chaining was tested and found to be fully operational. The DACs are mounted on the other side of the stand. The cables connecting the DACs and the RIS modules are routed through a hole in the backplate. The supply voltage of the DACs is provided by a DC power supply placed on the floor right next to the RIS stand.

Lastly, a computer is connected to the DAC, spindle and rotation control units, and the vector network analyzer. Thus, the measurements are automated.

For this thesis, two RIS modules were assembled. Both were measured by themselves first, then an RIS module with no diodes and lastly an up-scaled RIS (1×2 modules).

Fig. 3.17: Photo of the used testbed for the RIS. The RIS is attached to a stand that can move on a linear spindle drive. The stand has a backboard with absorbers (dark blue). The DACs controlling the RIS modules are placed behind this backboard. The supply voltage for the DACs is taken from a power supply placed on the floor. More absorbers are used on the spindle drive (light blue in front of the RIS) and on special rack behind the RIS stand (dark gray). The vector network analyzer ZVA 24 from Rohde & Schwarz is connected to two horn antennas that can be rotated and moved via spindle and rotation drives. Lastly, the whole testbed is connected to a PC for automated measurements.

All measurements were made with the antennas pointing directly at the RIS. The angle at which the antennas were pointed at the RIS was kept constant at 15°. For each measured RIS variant, four different positions were used. These positions differ only by the distance between the antennas and the RIS. In all positions the antenna angle remains the same and both antennas are equidistant from the RIS (see Figure 3.18). Table 3.2 shows the distances d for the four measurement positions.

The only RIS pattern used in all tested RISs is that all cell groups have the same bias voltage. In this way, no beamforming occurs and the bulk of the signal is reflected according to Snell's law. This is why the measurement positions are set up for specular reflection. The bias voltage is set to 27 different values in total for each position. The voltages are

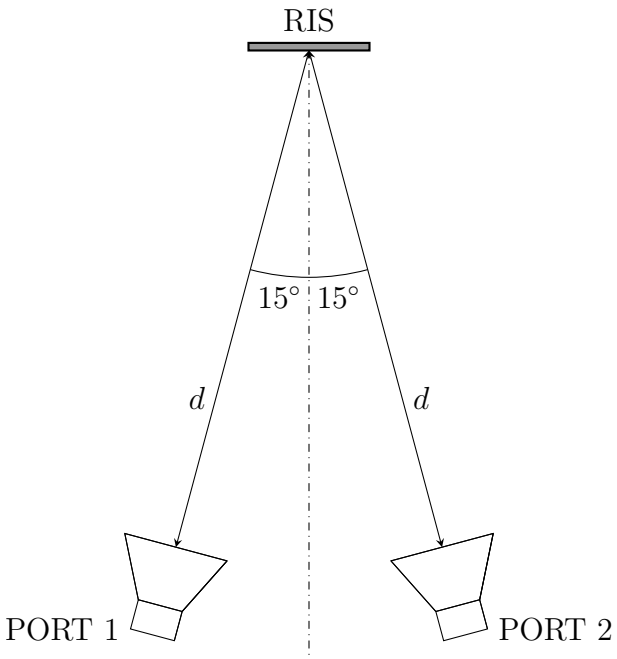

Fig. 3.18: Visualization of the positions of the antennas and the tested RIS in the measurements: top view. Note that both antennas are pointed directly at the center of the RIS. The angles at which the antennas are positioned are both 15°.

$$U_{bias}[\mathrm{V}] \in \{0;\ 1;\ 2;\ 3;\ 4;\ 4.2;\ 4.25;\ 4.5;\ 4.75;\ 5;\ 5.25;\ 5.3;\ 5.5;\ 5.75;\ 6;\ 6.25;\ 6.5;\ 6.6;\ 6.75;\ 7;\ 7.25;\ 7.5;\ 7.6;\ 7.75;\ 8;\ 9;\ 9.5\}.$$

The VNA measures S_{21} (the RIS reflection path coefficient) in the frequency band from 4.6 GHz to 6 GHz. The step size is 1 MHz and the measurement bandwidth is set to 10 kHz. Each sweep is repeated ten times for all bias voltage settings at all positions. In total, for one tested RIS, $10 \cdot 27 \cdot 4 = 1080$ frequency sweeps are performed.

Position	1	2	3	4
d [m]	1.64	1.89	2.15	2.41

Table 3.2: The distances d of the antennas from the measured RIS at the chosen positions.

3.5.2 Measurement of a single RIS module

In this section, the results obtained from measuring a single RIS module are discussed. The measurement was carried out as was described earlier. There were four positions (see Figure 3.18 and Table 3.2), one RIS pattern (all cells always have the same bias voltage), and 27 different bias voltage values. The frequency interval from 4.6 GHz to 6 GHz was measured. In Figure 3.19 a photo of the measured RIS module mounted on the stand is shown.

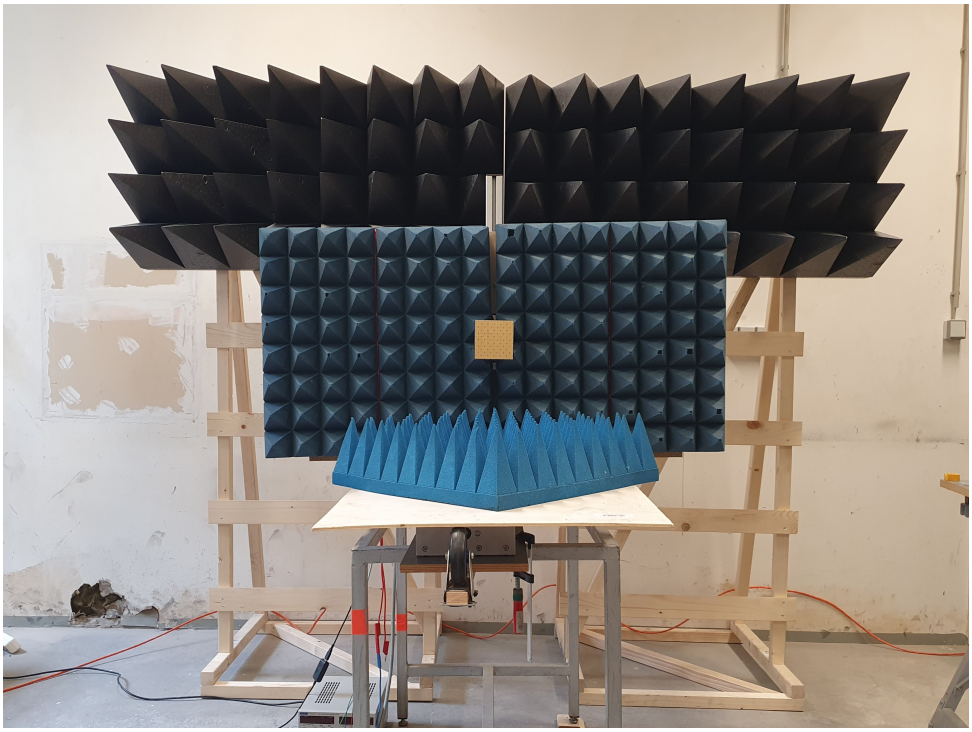

Fig. 3.19: Photo of a single RIS module mounted on the measurement stand. Front view.

The measured data are mainly represented in their complex form in the complex plane. The phase of the measured S_{21} is mainly given by the length of the RIS channel since the reference planes of the measurements are at the antenna inputs. Small deviations are not easily seen when the phase is plotted by itself. For this reason, most plots are in the complex plane.

Figure 3.20 shows the magnitude $|S_{21}|$ in the frequency band chosen for seven bias voltages. These U_{bias} are the same as in the simulations (except for 21 V). The measured magnitude exhibits a very similar behavior to the simulations in Figure 3.9. The tuning of the resonance is clearly visible, and even the secondary resonances can be seen. There seems to be a frequency shift of circa 100 MHz.

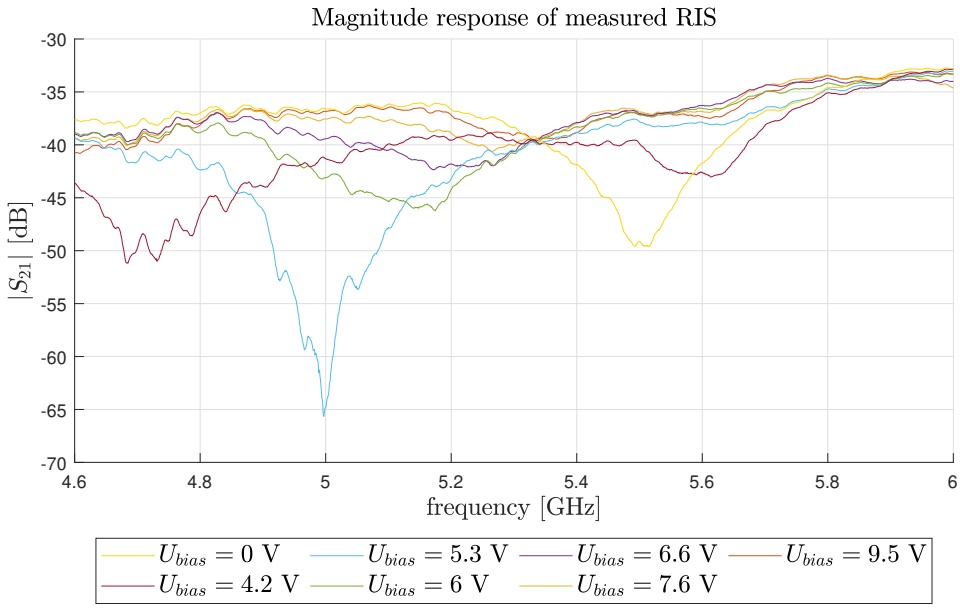

Fig. 3.20: Measurement of single RIS module. Magnitude of the measured S_{21} for 7 chosen values of U_{bias}.

Figure 3.21 shows the measured S_{21} at 5 GHz for the positions chosen while changing the bias voltage U_{bias}. The S_{21} for $U_{bias} = 0$ V is plotted as a dot. As mentioned above, a measurement of an RIS module with no varactor diodes connected was also done. The measured S_{21} of this non-assembled RIS module are plotted as single "X" markers in the color that corresponds to the correct measurement position. These data are called "static S_{21}" for the remainder of this thesis.

The measured S_{21} have the shape of an elliptical crescent. The shape is consistent across all positions. Since the distance between the RIS and the antennas changes, the crescents rotate and become progressively smaller as the distance d increases. For all four positions, the static component S_{21} are inside the crescents. Moreover, the origin of the complex plane is also within all four crescents.

The author of [29] found that there is a static and dynamic component to the reflection coefficient Γ of the RIS: $\Gamma = \Gamma_S + \Gamma_D$. In his work, he used the S_{21} at $U_{bias} = 0$ V as the static part. In this thesis, the static component is defined from now on by the reflection, when the diode contacts are disconnected; open circuit. This can only be measured when no diodes are placed on the RIS module. This static component then defines the reference for the tunable phases of the RIS.

In order to calculate the dynamic reflection coefficient Γ_D of the RIS, the raw S_{21} data need to be processed. The S_{21} is defined by the entire RIS path: a cascade of

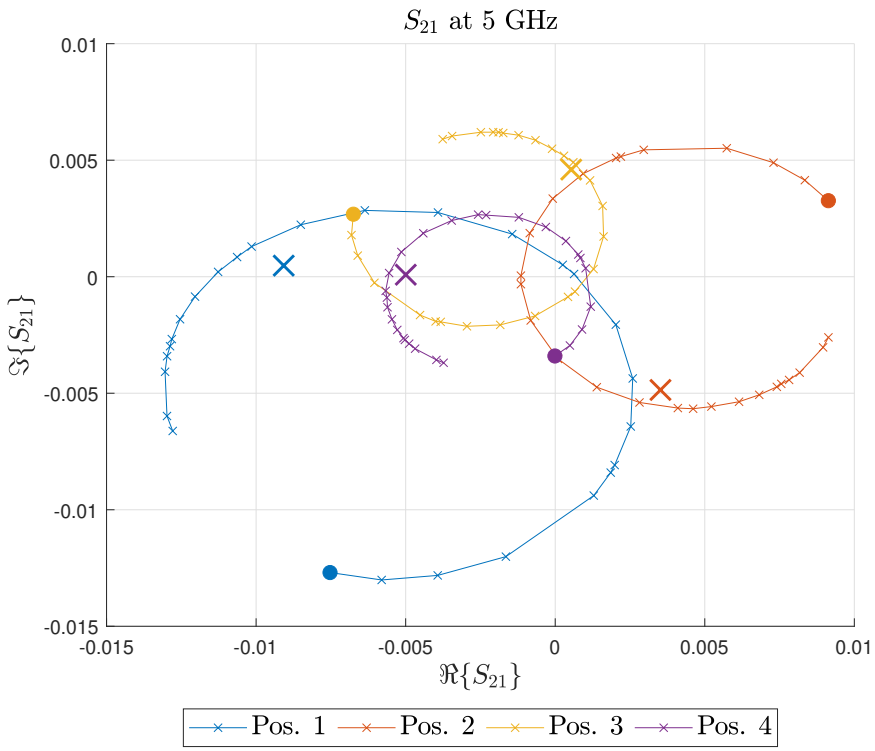

Fig. 3.21: Measurement of single RIS module. Raw data S_{21} at 5 GHz when sweeping the bias voltage for the four positions. The dots are the S_{21} values when $U_{bias} = 0$ V for each position, and then the points are in ascending order of U_{bias}. The static S_{21} measured (an RIS module without diodes) are plotted as big letters "X" in the given position color.

the transmitter-to-RIS path response $A(f)$, RIS reflection coefficient $\Gamma(f)$ and the RIS-to-receiver path response $B(f)$. A simplified version of the channel model from [29] is used. $A(f)$ is given by the product of the gain g of the port 1 antenna and the free space path with length d. Similarly, $B(f)$ is given by the product of the gain g of the port 2 antenna (with correction parameter f_c/f) and the free space path with length d. The gain is the same for both antennas $g = 18$ dBi. The responses of the partial paths are found to be

$$A(f) = \frac{\sqrt{g(f)}}{\sqrt{4\pi}d} \exp\left(\frac{-j2\pi f d}{c_0}\right),$$
$$B(f) = \frac{f_c}{f}\frac{\sqrt{g(f)}}{\sqrt{4\pi}d} \exp\left(\frac{-j2\pi f d}{c_0}\right).$$

The RIS channel model can be expressed as

$$S_{21}(f, U_{bias}) = A(f)\Gamma(f, U_{bias})B(f) + \widetilde{W} \tag{3.1}$$

where noise $\widetilde{W}$ is assumed AWGN.

The processing of S_{21} is done in three steps. First, we average the data. Each measurement has been repeated multiple times; averaging these repetitions minimizes the noise component. The static S_{21} is then subtracted from the data, and then the data are divided by the channel responses $A(f)$ and $B(f)$ for the given frequency and position. Since both channel responses have complex values, the division rotates and scales the data around the origin. These processed data represent the dynamic reflection coefficient Γ_D. For a more detailed description of the processing and channel model, refer to [29].

The dynamic coefficient for a single RIS module at 5 GHz placed at position 1 is shown in Figure 3.22. The origin of the complex plane is within the crescent of Γ_D. The crescent is approximately $7.5 \cdot 10^{-3}$ [−] wide and $7.7 \cdot 10^{-3}$ [−] high. The magnitude of the dynamic reflection coefficient is the smallest at bias voltages of 6.25 V to 6.5 V. The crescent of Γ_D is much smaller than in the simulation (Fig. 3.7). The leading cause of this is the over spill of the signal transmitted from antenna 1. This over spill is unavoidable since the RIS is illuminated by the main lobe and the beam width needs to be larger than the RIS, otherwise the different unit cells would be illuminated with different antenna gains.

The size of the tunable phase interval is 326°. The relation between the applied bias voltage and the reflection phase is taken from the dynamic reflection Γ_D and displayed in the tuning diagram of the RIS module in Figure 3.23. The tuning diagram has the same overall shape as the simulated version. Although there are slight differences, the tuning diagram of the manufactured RIS module is a good match to the simulated case. For better insight into the cause of the differences, more precise simulations with a RIS module of finite size could be made in the future.

The measured S_{21} data of the proposed RIS module are compared to the previous RIS in Figure 3.24. The data displayed are taken from measurements at position 1 at 5 GHz. The most noticeable difference is the shape. While the S_{21} of the proposed design has a crescent shape, the S_{21} of the previous design has a spiral shape. In this figure, the existence of a static component is very apparent. If there were no static components, the spiral S_{21} of the previous RIS would be expected around the origin. Concrete information on the tunable phases and the magnitudes of the dynamic reflection coefficient of the previous RIS could not be obtained, since the static component could not be measured. However, if we assume that the static S_{21} is inside the spiral, then the size of the tunable phase interval would be greater

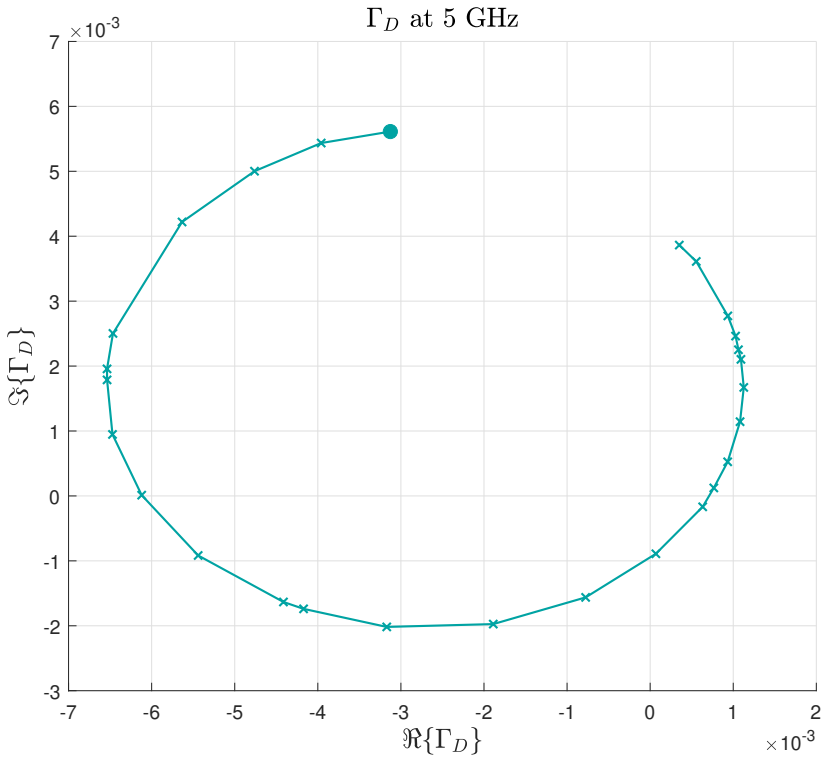

Fig. 3.22: Measurement of single RIS module. Dynamic reflection coefficient Γ_D at 5 GHz at position 1: sweeping bias voltage. The dot is the value of Γ_D for $U_{bias} = 0$ V, and then the points are in ascending order of U_{bias}. The origin of the complex plane is given by the static component measured.

than 360°, but the magnitudes would be much smaller compared to the proposed RIS. On the other hand, if we assume that the static S_{21} is outside the spiral, then the magnitudes are greater than in the previous case, but the tunable phase interval shrinks significantly.

Lastly, how the measured S_{21} changes with frequency is explored. Figure 3.25 shows the measured S_{21} of the RIS module at position 1 for different frequencies. The static S_{21} is also plotted as a large "X". For frequencies up to 5.6 GHz the S_{21} has a crescent shape. At higher frequencies, it curls up into itself. The crescents are rotated differently because the wavelength is different, so the path has a different electrical length. However, the static component changes its position relative to the crescent. At 5 GHz the static S_{21} is close to the S_{21} for $U_{bias} = 6.5$ V, it moves closer to the S_{21} for 0 V. It exits the crescent at 5.4 GHz and remains outside. This means that the tunable phase interval gets significantly smaller. Also note that from 5.6 GHz the S_{21} do not surround the complex plane origin anymore. The crescents are larger around 5.3 to 5.4 GHz.

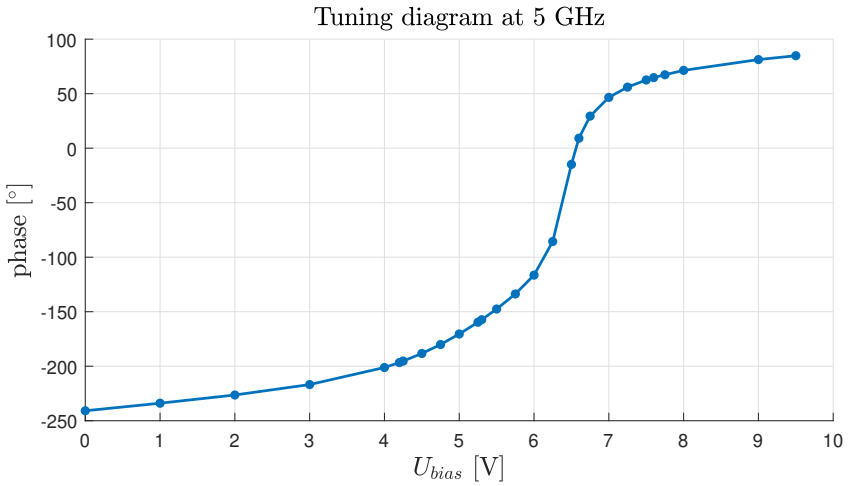

Fig. 3.23: Single RIS module tuning diagram (dependence of the reflection phase on the bias voltage applied) at operation frequency 5 GHz.

It is evident from Figure 3.25 that the dynamic component changes with frequency. Since the static component changes its position in relation to the data, the tunable phases and the magnitudes of the dynamic component also change. The question of how to define the optimal operating frequency and the operation bandwidth can be explored further in the future.

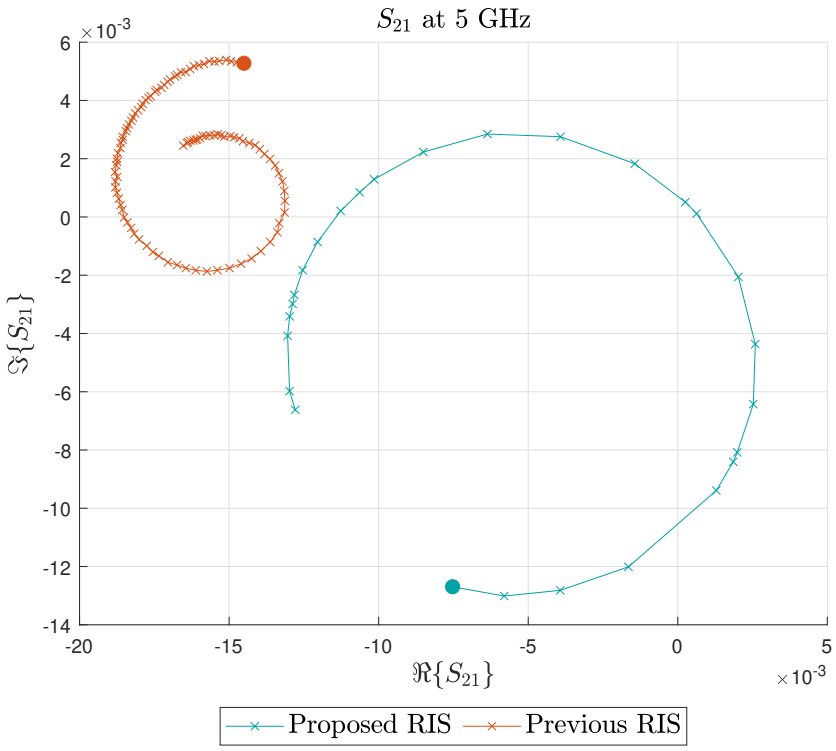

Fig. 3.24: Single RIS module compared to the previous RIS design. S_{21} at 5 GHz at position 1: sweeping bias voltage U_{bias}. The dots are the S_{21} values for $U_{bias} = 0$ V, and then the points are in ascending order of U_{bias}.

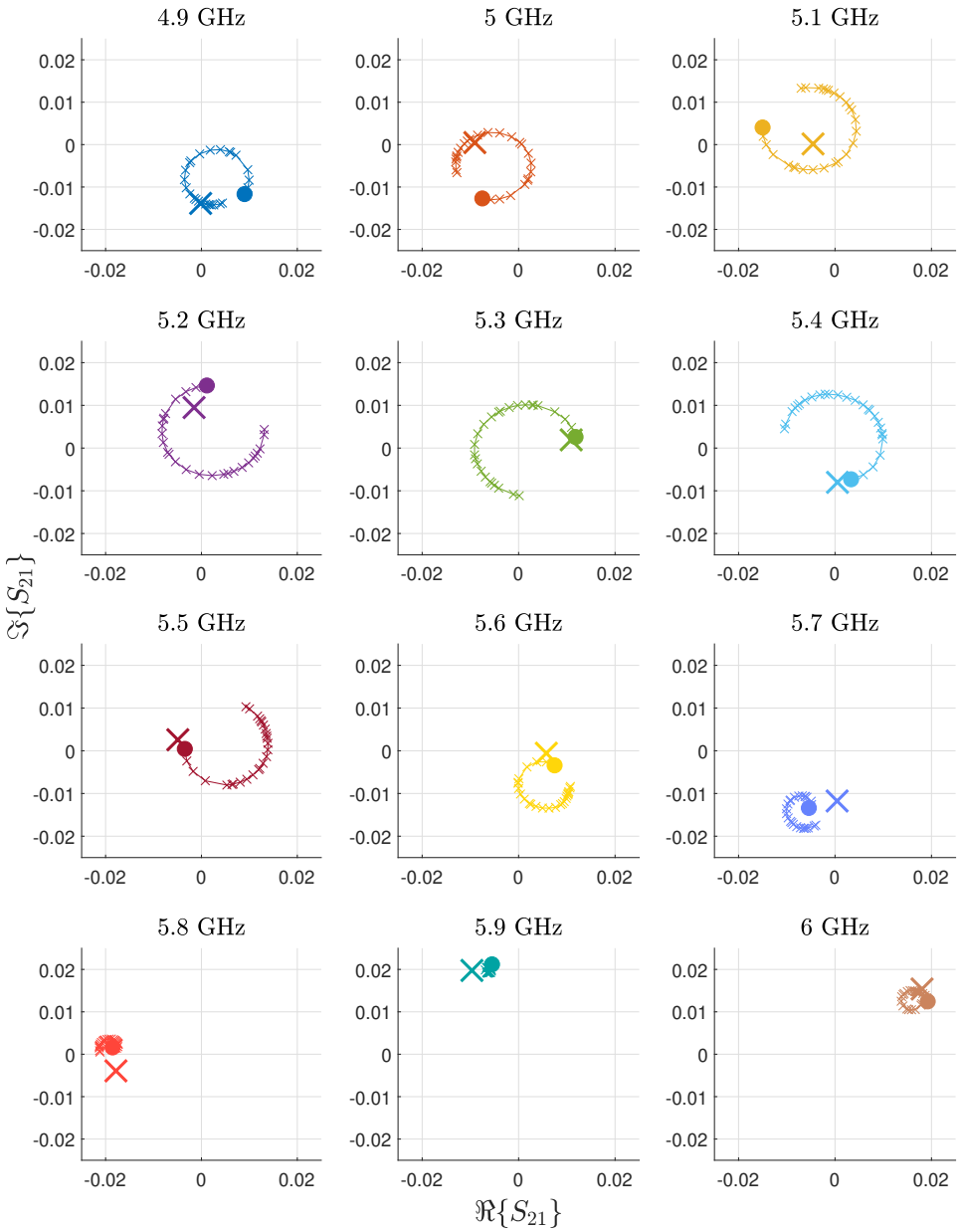

Fig. 3.25: Single RIS module S_{21} at position 1 for different frequencies in the complex plane. As in previous figures, the dot is the value of $U_{bias} = 0$ V and the larger "X" is the respective static component.

3.5.3 Measurement of an up-scaled RIS

This section presents the results of measuring an up-scaled RIS. The measurement setup remains the same as for a single RIS module. The up-scaled RIS consists of two RIS modules in a 1×2 configuration. The up-scaled RIS is shown in Figure 3.26.

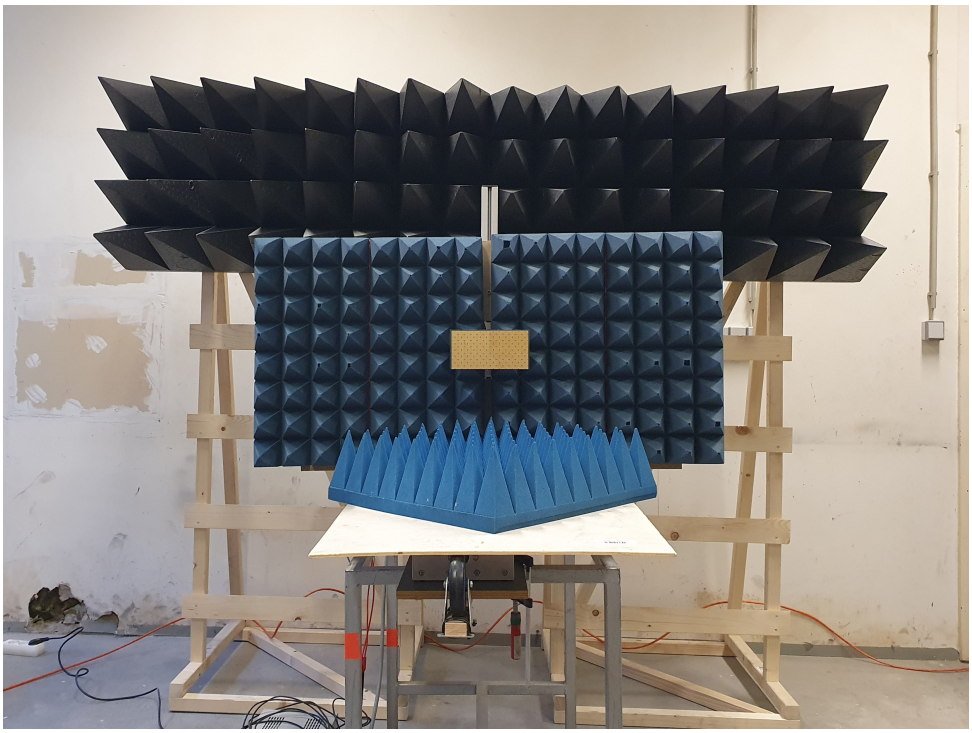

Fig. 3.26: Photo of the up-scaled RIS mounted on the measurement stand. Front view.

In Figure 3.27 the magnitude $|S_{21}|$ is shown for seven chosen values of U_{bias}. The magnitude responses are very similar to the single RIS module measurement (Fig. 3.20). Only for the up-scaled RIS, the magnitudes are greater by almost 6 dB. This increase is caused by the larger surface of the RIS. The up-scaled RIS has twice the size, so a magnitude increase of 6 dB, in the optimal case, is expected. In all other aspects, the magnitude responses can be considered equal.

The raw S_{21} data at 5 GHz at the chosen positions is shown in Figure 3.28. The static component is also plotted. However, the static S_{21} for an up-scaled RIS could not be measured, thus the static component measured for a single module is used. Therefore, it is not certain whether the phases of the dynamic component of the up-scaled RIS are entirely correct. For the comparisons in this thesis, the static S_{21} of a single module is sufficient. In the future, static components of up-scaled RISs in different configurations can be measured to better estimate tuning performance and increase measurement precision.

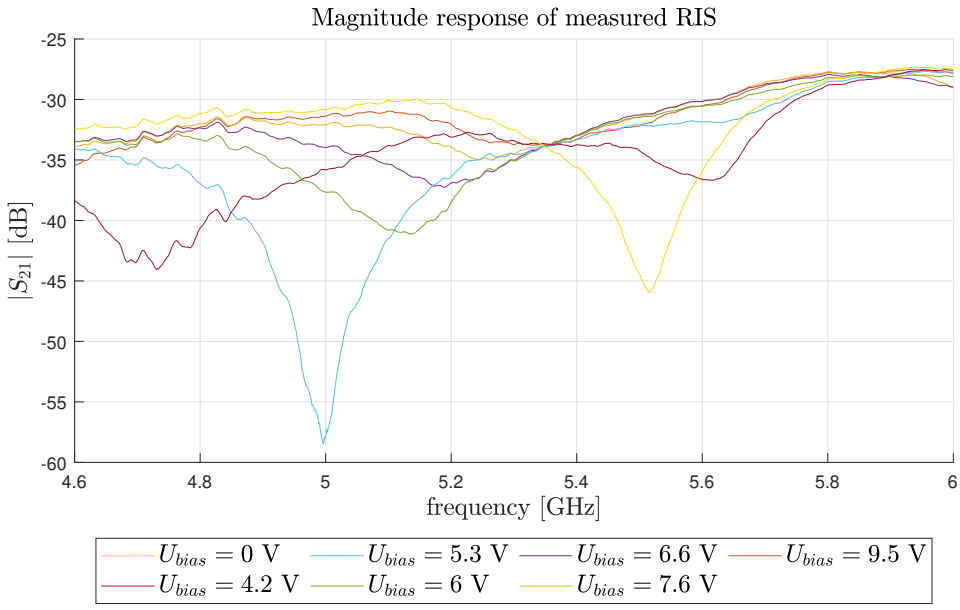

Fig. 3.27: Measurement of up-scaled RIS. Magnitude of the measured S_{21} for 7 chosen values of U_{bias}.

The measured S_{21} once again has a crescent shape at all positions. The crescents rotate and become smaller with increasing antenna to RIS distance d. Again, the crescents all surround the origin of the complex plane and their respective static component.

Figure 3.29 shows the dynamic component Γ_D of the up-scaled RIS at position 1 at the operating frequency. The dynamic component is calculated from the raw S_{21} data in the way described in Subsection 3.5.2. The crescent is approximately $14.2 \cdot 10^{-3}$ [–] wide and $14.5 \cdot 10^{-3}$ [–] high, nearly twice the size of the single RIS module crescent. Like in the case of a single module, Γ_D surrounds the origin. Therefore, the phase can be tuned very freely with the bias voltage. The size of the tunable phase interval is 319°, slightly smaller than for the single module. This difference is most likely given by using the static component of the single RIS module for the up-scaled RIS.

The tuning diagram derived from the dynamic component Γ_D is shown in Figure 3.30. The steep part of the tuning diagram moved down by approximately 0.5 V, probably caused by the static component used.

The up-scaled RIS is compared with the single RIS modules in Figure 3.31. The figure shows the dynamic component Γ_D of both created RIS modules and the up-scaled RIS. The difference in size is apparent. The up-scaled RIS clearly reflects

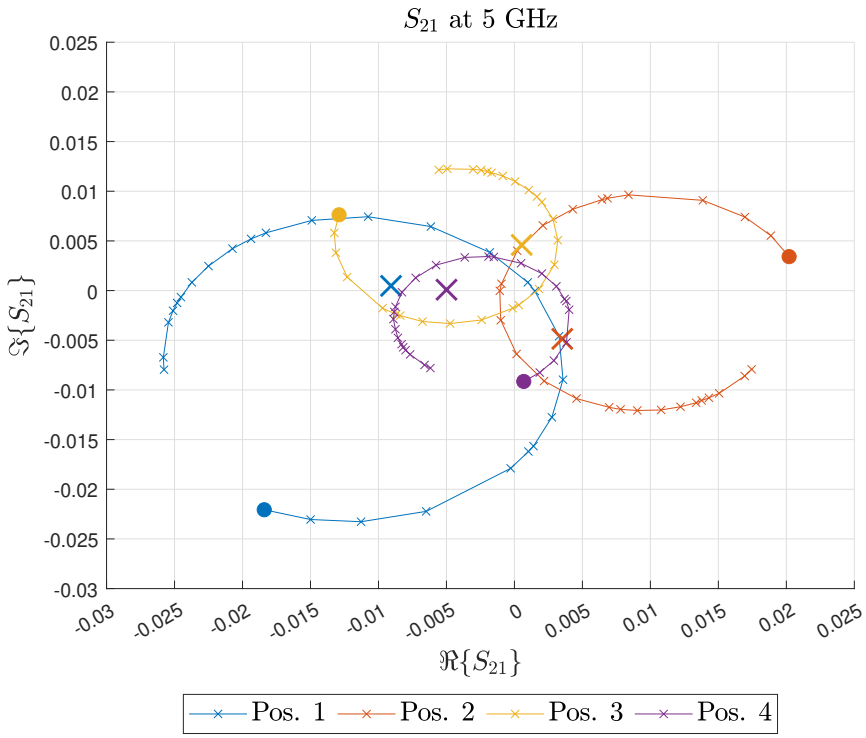

Fig. 3.28: Measurement of Up-scaled RIS. Raw data S_{21} at 5 GHz when sweeping the bias voltage for the four positions. The dots are the S_{21} values when $U_{bias} = 0$ V for each position, and then the points are in ascending order of U_{bias}. The static S_{21} measured (an RIS module without diodes) are plotted as big letters "X" in the given position color.

more of the transmitted signal and boosts the RIS path more than just a single RIS module. The rotation of the crescents is practically identical for all three cases.

The crescents of the two modules do not completely overlap. The measurements of the static component and the two modules were performed on different days. Differences in temperature, outside interference, or small movements of the antennas or RIS could all have contributed to this. However, all things considered, the dynamic behavior of the two modules is practically identical.

Lastly, the change of the S_{21} of the up-scaled RIS with frequency is investigated. Figure 3.32 shows the S_{21} at measurement position 1 over the measured frequency bandwidth. The behavior of S_{21} is identical to that in the single-module case. The S_{21} has a crescent shape up to 5.6 GHz. For frequencies from 5 to 5.5 GHz, the crescent surrounds the origin of the complex plane. The static component is first inside the crescent but changes its position with frequency until it leaves the crescent

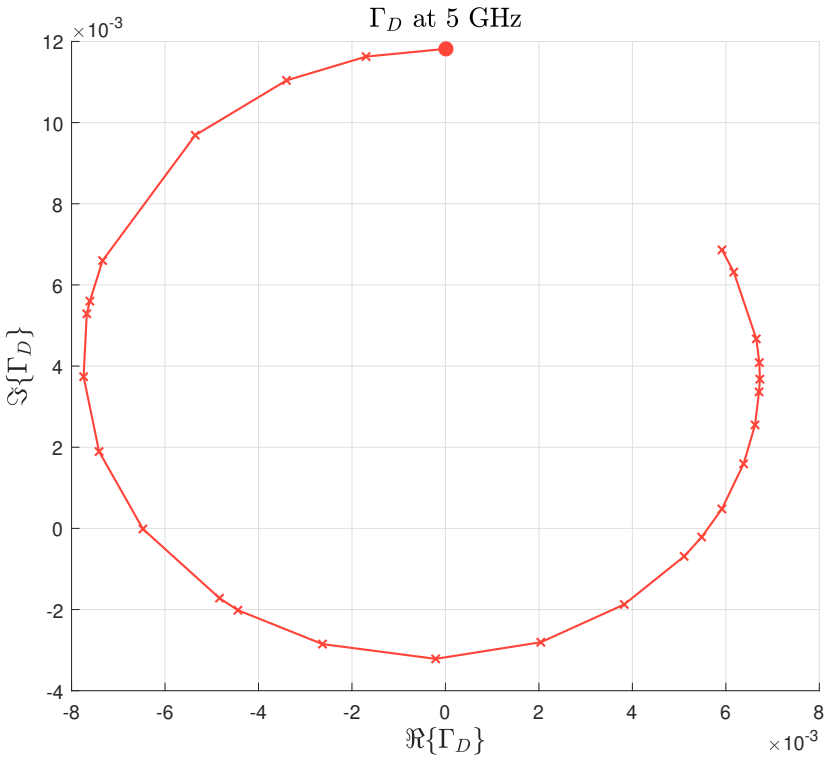

Fig. 3.29: Measurement of an up-scaled RIS. Dynamic reflection coefficient Γ_D at 5 GHz at position 1: sweeping bias voltage. The dot is the value of Γ_D for $U_{bias} = 0$ V, and then the points are in ascending order of U_{bias}. The origin of the complex plane is given by the static component measured.

at 5.6 GHz. The crescents are largest at 5.3 GHz to 5.4 GHz At 5.7 GHz and higher the S_{21} curls up.

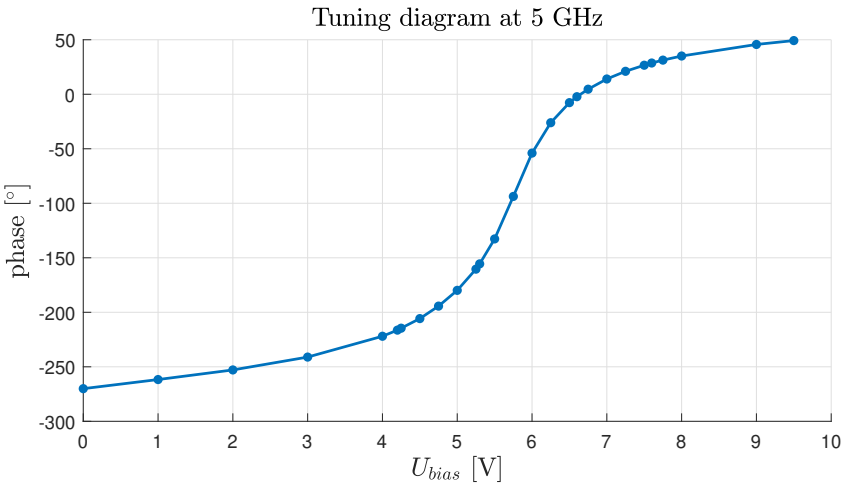

Fig. 3.30: Up-scaled RIS tuning diagram (dependence of the reflection phase on the bias voltage applied) at the operating frequency 5 GHz.

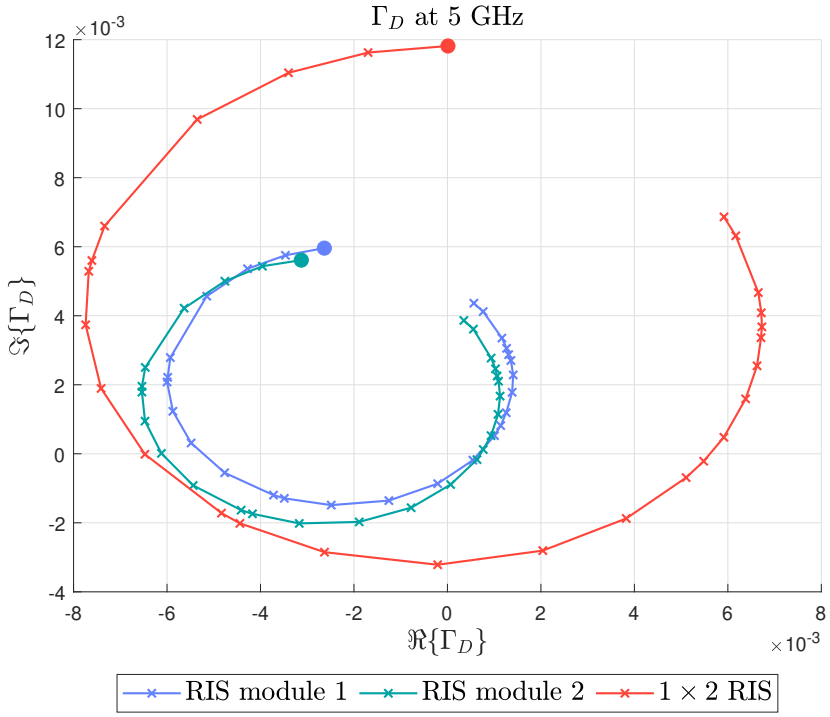

Fig. 3.31: Comparison of the up-scaled RIS to single modules. Dynamic reflection coefficient Γ_D at 5 GHz at position 1: sweeping bias voltage. The dot is the value of Γ_D for $U_{bias} = 0$ V, and then the points are in ascending order of U_{bias}. The origin of the complex plane is given by the static component measured.

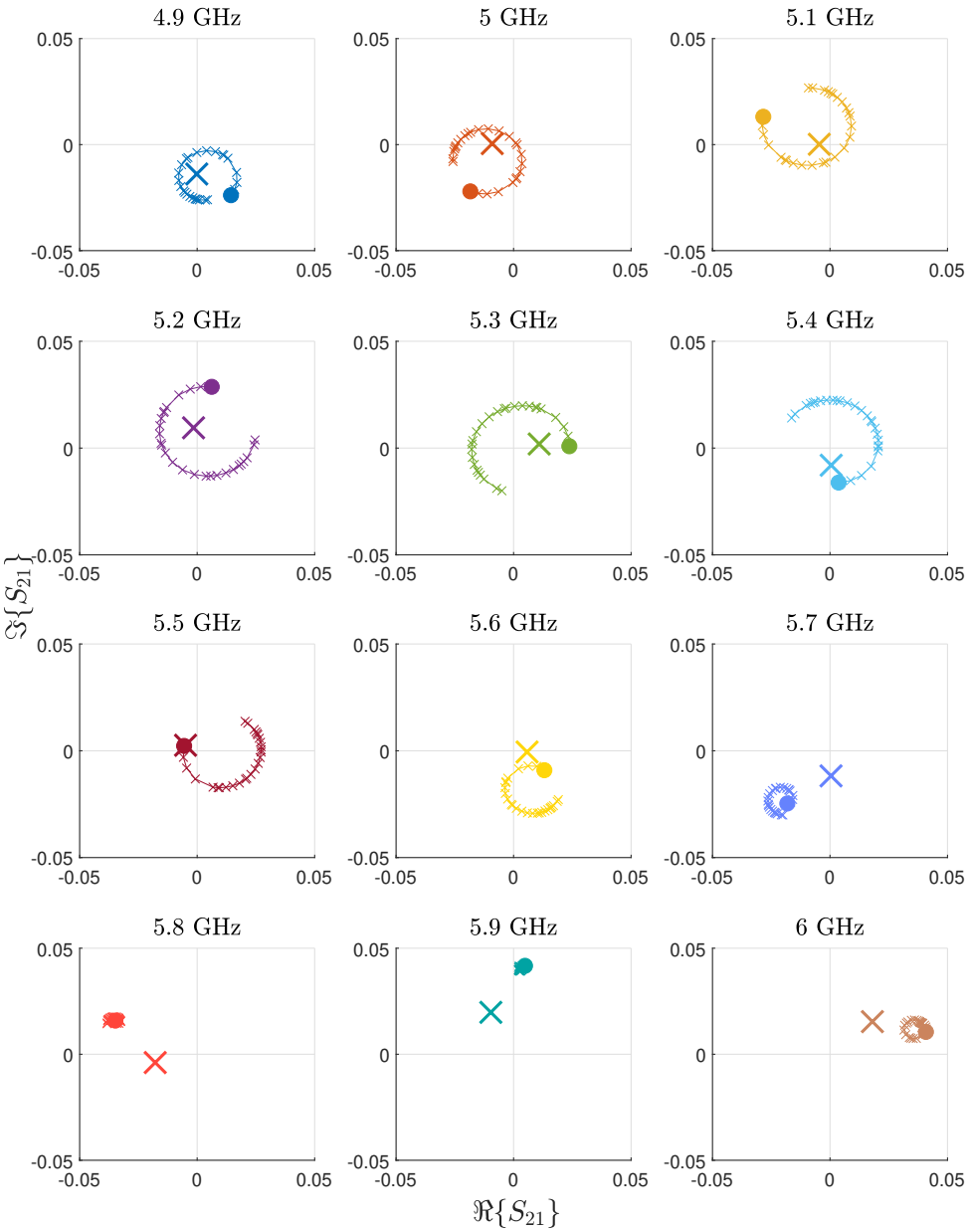

Fig. 3.32: Up-scaled RIS S_{21} at position 1 for different frequencies in the complex plane. As in previous figures, the dot is the value of $U_{bias} = 0$ V and the larger "X" is the respective static component.

Discussion & Outlook

This section provides a discussion of the proposed RIS design. The features, measured characteristics, and research applications of the RIS design are addressed.

The tested RIS modules behave in a manner consistent with the simulations. This can be easily seen in the magnitude responses and also in the dynamic reflection plots. The magnitude responses show that the bias voltage tunes the primary resonance. Moreover, secondary resonances are also present.

The dynamic reflection coefficient Γ_D has the same crescent shape as in the simulations. The different sizes of the crescents between the measurements and the simulation are mainly given by the over spill of the signal transmitted from the antenna to the RIS.

The tunable phase ranges and tuning diagrams of the manufactured and simulated RIS modules also match quite well. The manufactured RIS modules enable the tuning of the reflection phase in a range of 326°. The results of both manufactured modules are practically the same, which speaks to the repeatability and consistency of the manufacturing of the RIS module design.

In summary, the manufactured RIS prototype modules are operational and can be used for further research. In the following, some examples of possible research are given.

The issue of beamforming can be investigated using the proposed RIS modules and the existing testbed. A simple setup with one antenna illuminating the RIS perpendicularly and the other positioned at a given angle. Then the tuning diagram provided by this thesis could be used to find the optimum pattern to maximize the signal received by the second antenna. This, of course, can also be done for a scaled-up RIS.

The scalable nature of the proposed RIS design is its greatest asset. The RIS modules can create many different scaled-up reconfigurable intelligent surfaces. The effect of the size and shape of the RIS module configuration on its behavior can be investigated, not unlike what was done in this thesis. With the added benefit of modularity, the RIS modules can also be used to create RISs in the shape of a corner or a rounded surface.

The biasing network of the RIS modules also allows each unit cell to be individually controlled. Thus, the effect of the number of controllable elements on the beamforming and beam steering performance can be explored, while the physical size of the RIS remains the same.

Another interesting research topic is the characterization of RISs. The underlying issue of how to determine the optimal operating frequency of an RIS and define the operating bandwidth remains largely unanswered. Linked to this question is the

question of how to define the best performance when it comes to RISs. The position of the static component in relation to the measured S_{21} data dictates the phases and magnitudes of the dynamic component Γ_D. The question is, what is the best position for the static component, ergo, where is the balance between having the biggest possible tunable phase range and having the biggest possible magnitudes for all bias voltages.

One possible improvement to the RIS module design is related to module mounting. The chosen mounting adapters are SMD components that do not have an alignment pin. This means that the distance between them is not always the same and depends on how the adapters move while reflow soldering. This can lead to small gaps and misalignment of the RIS modules when mounted. Choosing a variant of the mounting adapter with an alignment pin solves this issue. The same could be done with the group and module connectors if needed. Adding alignment pins would require additional PCB manufacturing steps, namely backdrilling.

The next steps in RIS research at the Institute of Telecommunications are already being taken. Two additional testbeds are currently being developed for RIS measurement validation.

The authors of [6] work on a testbed that allows the receiving antenna to rotate around the RIS and the RIS to be tilted up and down, thus scanning the rotation and elevation angles of the reflected waves. The other testbed is being developed as part of a bachelor's thesis. This testbed focuses on bringing RIS measurements into an anechoic chamber. The testbed features a stand for the RIS that is made of material with $\varepsilon_r \approx 1$ (so it does not interfere with wave propagation) and a communication channel for the RIS controller compatible with the anechoic chamber.

In conclusion, the manufactured RIS prototype modules are operational and can be used to explore many research topics with the existing testbed. In addition, more testbeds for RIS measurements are being developed, which expand the possible applications of the RIS prototype.

4 Conclusion

The aim of this thesis is to design, manufacture, and characterize an improved and scalable RIS module by measurements based on previous work [5], [28]. The RIS module is required to support side-by-side installation to construct an up-scaled reconfigurable intelligent surfaces.

The previous RIS design was reviewed and used as the basis for a redesign. Side-by-side installation is enabled by a borderless RIS module geometry. To make the RIS module borderless, the biasing network and mounting adapters were placed on the module's backside. The unit cells were redesigned to accommodate a new four-layer stackup of the RIS module PCB. The resulting RIS module with 6×6 unit cells is easily mounted in many different configurations. All unit cells can be biased individually.

Two RIS modules were manufactured and tested, and shown to be fully operational by measurements. In addition, the performance of the two RIS modules was the same. This means that more modules can be manufactured with consistent results.

At the operation frequency 5 GHz, the reflection phase is tunable over a range of 326° with bias voltages ranging from 0 V to 9.5 V. An up-scaled RIS consisting of two RIS modules side-by-side was also constructed and measured. The up-scaled RIS has practically the same characteristics as a single module, except for a much larger magnitude of steerable reflection. The up-scaled surface area leads to an almost doubled magnitude of the reflected signal. In this way, the present RIS design shows significant improvements over the previous design [5], [28].

The functional and easy-to-use RIS modules may prove useful to answer many major RIS research questions mentioned in this thesis. The measured characteristics are available for comparisons with increasingly more accurate RIS models to benchmark their goodness of fit. In addition, the RIS modules can be used in the validation of channel models in different scenarios (indoor, outdoor, non-LOS, LOS,...). With the option to control each unit cell individually, the RIS modules allow to efficiently investigate and optimize RIS configurations. The influence of increasing the number of controllable elements, increased RIS surface area and various optimization techniques can be explored in the future.

Some of the open issues are immediately addressable. Firstly, there is the question of defining the operational bandwidth of the RIS modules. The reflection of the RIS changes with frequency. Not only does the tunable phase range change, but also the reflection's magnitude. Investigating these variabilities and specifying the frequencies with adequate performance is key to finding the operational bandwidth. Another option is to implement a simple beamforming setup with the RIS

modules and the provided tuning diagram and measure the achievable increase in signal strength. In addition, since the RIS design is scalable and has an adjustable biasing network, it is feasible to explore scaling effects of the RIS size, different shapes of reconfigurable intelligent surfaces, beam control strategies, behavioral channel models, cross-polarization effects, to name a few.

Ultimately, the RIS modules developed in this thesis contribute to a deeper understanding of reconfigurable intelligent surfaces and controllable wireless channels. Gaining insight into the underlying principles and design improvements of RIS technology may pave the way for its integration into future wireless communication networks. In time, reconfigurable intelligent surfaces could become part of our daily lives without us noticing it.

Bibliography

[1] E. Björnson, H. Wymeersch, B. Matthiesen, P. Popovski, L. Sanguinetti, and E. de Carvalho, "Reconfigurable intelligent surfaces: A signal processing perspective with wireless applications," *IEEE Signal Processing Magazine*, vol. 39, no. 2, pp. 135–158, 2022. DOI: 10.1109/MSP.2021.3130549.

[2] Y. Liu, X. Liu, X. Mu, *et al.*, "Reconfigurable intelligent surfaces: Principles and opportunities," *IEEE Communications Surveys & Tutorials*, vol. 23, no. 3, pp. 1546–1577, 2021. DOI: 10.1109/COMST.2021.3077737.

[3] E. Basar, M. Di Renzo, J. De Rosny, M. Debbah, M.-S. Alouini, and R. Zhang, "Wireless communications through reconfigurable intelligent surfaces," *IEEE Access*, vol. 7, pp. 116 753–116 773, 2019. DOI: 10.1109/ACCESS.2019.2935192.

[4] H. Jiao, H. Liu, and Z. Wang, "Reconfigurable intelligent surfaces aided wireless communication: Key technologies and challenges," in *2022 International Wireless Communications and Mobile Computing (IWCMC)*, 2022, pp. 1364–1368. DOI: 10.1109/IWCMC55113.2022.9824117.

[5] S. Zhao, R. Langwieser, and C. F. Mecklenbraeuker, "Reconfigurable digital metasurface for 3-bit phase encoding," in *WSA 2021; 25th International ITG Workshop on Smart Antennas*, 2021, pp. 1–6. [Online]. Available: https://ieeexplore.ieee.org/abstract/document/9739088.

[6] F. Kiss, R. Langwieser, R. Prüller, H. Groll, S. Zhao, and M. Rupp, "Measurement environment for ris enhanced wireless channels," in *2023 IEEE 24th International Workshop on Signal Processing Advances in Wireless Communications (SPAWC)*, 2023, pp. 381–385. DOI: 10.1109/SPAWC53906.2023.10304485.

[7] C. Huang, C. Zhang, J. Yang, *et al.*, "Reconfigurable metasurface for multifunctional control of electromagnetic waves," *Advanced Optical Materials*, vol. 5, no. 22, 1700485f, 2017. DOI: 10.1002/adom.201700485. [Online]. Available: https://advanced.onlinelibrary.wiley.com/doi/abs/10.1002/adom.201700485.

[8] C. Huang, A. Zappone, G. C. Alexandropoulos, M. Debbah, and C. Yuen, "Reconfigurable intelligent surfaces for energy efficiency in wireless communication," *IEEE Transactions on Wireless Communications*, vol. 18, no. 8, pp. 4157–4170, 2019. DOI: 10.1109/TWC.2019.2922609.

[9] D. F. Sievenpiper, "Artificial impedance surfaces for antennas," in *Modern Antenna Handbook*. John Wiley & Sons, Ltd, 2008, ch. 15, pp. 737–777, ISBN: 9780470294154. DOI: 10.1002/9780470294154.ch15.

[10] O. Tsilipakos, A. C. Tasolamprou, A. Pitilakis, *et al.*, "Toward intelligent metasurfaces: The progress from globally tunable metasurfaces to software-defined metasurfaces with an embedded network of controllers," en, *Adv. Opt. Mater.*, vol. 8, no. 17, p. 2 000 783, Sep. 2020. DOI: 10.1002/adom.202000783.

[11] J. Wang, W. Tang, J. C. Liang, *et al.*, "Reconfigurable intelligent surface: Power consumption modeling and practical measurement validation," *IEEE Transactions on Communications*, vol. 72, no. 9, pp. 5720–5734, 2024. DOI: 10.1109/TCOMM.2024.3382332.

[12] N. Afzali, M. J. Omidi, K. Navaie, and N. S. Moayedian, "Low complexity multi-user indoor localization using reconfigurable intelligent surface," in *2022 30th International Conference on Electrical Engineering (ICEE)*, 2022, pp. 731–736. DOI: 10.1109/ICEE55646.2022.9827014.

[13] H. Feng and Y. Zhao, "Indoor enhancement of mmwave based on reconfigurable intelligent surface: Irs or df relay connection?" In *2022 IEEE 96th Vehicular Technology Conference (VTC2022-Fall)*, 2022, pp. 1–6. DOI: 10.1109/VTC2022-Fall57202.2022.10012916.

[14] Z. Fu, X. Zou, Y. Liao, G. Lai, Y. Li, and K. L. Chung, "A brief review and comparison between transmitarray antennas, reflectarray antennas and reconfigurable intelligent surfaces," in *2022 IEEE Conference on Telecommunications, Optics and Computer Science (TOCS)*, 2022, pp. 1192–1196. DOI: 10.1109/TOCS56154.2022.10016145.

[15] Z. Sattar and A. Haghighat, "Nearly passive reconfigurable intelligent surface with constant phase-shifts," in *2021 IEEE 32nd Annual International Symposium on Personal, Indoor and Mobile Radio Communications (PIMRC)*, 2021, pp. 794–799. DOI: 10.1109/PIMRC50174.2021.9569529.

[16] Z. Zhang, L. Dai, X. Chen, *et al.*, "Active ris vs. passive ris: Which will prevail in 6g?" *IEEE Transactions on Communications*, vol. 71, no. 3, pp. 1707–1725, 2023. DOI: 10.1109/TCOMM.2022.3231893.

[17] H.-T. Chen, A. J. Taylor, and N. Yu, "A review of metasurfaces: Physics and applications," *Rep. Prog. Phys.*, vol. 79, no. 7, p. 076 401, Jul. 2016. DOI: 10.1088/0034-4885/79/7/076401.

[18] J. Huang and R. Pogorzelski, "A ka-band microstrip reflectarray with elements having variable rotation angles," *IEEE Transactions on Antennas and Propagation*, vol. 46, no. 5, pp. 650–656, 1998. DOI: 10.1109/8.668907.

[19] C. Lee, P. Mak, and A. DeFonzo, "Optical control of millimeter-wave propagation in dielectric waveguides," *IEEE Journal of Quantum Electronics*, vol. 16, no. 3, pp. 277–288, 1980. DOI: 10.1109/JQE.1980.1070468.

[20] T. Nagai, H. Takahashi, R. Okazaki, K. Tanabe, I. Terasaki, and H. Taniguchi, "Optical control of dielectric permittivity in laal0.99zn0.01o3-δ," *Applied Physics Letters*, vol. 110, no. 17, p. 172 901, Apr. 2017, ISSN: 0003-6951. DOI: 10.1063/1.4979644. eprint: https://pubs.aip.org/aip/apl/article-pdf/doi/10.1063/1.4979644/19780312/172901_1_online.pdf. [Online]. Available: https://doi.org/10.1063/1.4979644.

[21] A. Sikder, V. Kumar, G. Srivastava, and A. Mohan, "A 2-bit polarization-insensitive reconfigurable intelligent surface for triple band," in *2024 Second International Conference on Microwave, Antenna and Communication (MAC)*, 2024, pp. 1–4. DOI: 10.1109/MAC61551.2024.10837426.

[22] C.-Y. Chang and H.-T. Chou, "A millimeter-wave binary reconfigurable intelligent surface on a low-cost fr4 substrate," in *2024 18th European Conference on Antennas and Propagation (EuCAP)*, 2024, pp. 1–4. DOI: 10.23919/EuCAP60739.2024.10501260.

[23] J. Du, B. Liu, C. H. Chan, and Q. Zhang, "A wideband reconfigurable reflective metasurface," in *2024 15th Global Symposium on Millimeter-Waves & Terahertz (GSMM)*, 2024, pp. 45–47. DOI: 10.1109/GSMM61775.2024.10552921.

[24] Y. Zhao, Y. Lu, J. Dai, Z. Luo, and Q. Cheng, "A fast inverse design method for reconfigurable intelligent metasurface based on generative model," in *2024 IEEE MTT-S International Wireless Symposium (IWS)*, 2024, pp. 1–3. DOI: 10.1109/IWS61525.2024.10713664.

[25] A. Abrardo, A. Toccafondi, and M. Di Renzo, "Analysis and optimization of reconfigurable intelligent surfaces based on s-parameters multiport network theory," in *2024 18th European Conference on Antennas and Propagation (EuCAP)*, 2024, pp. 1–4. DOI: 10.23919/EuCAP60739.2024.10501476.

[26] H. Radpour, M. Hofer, L. W. Mayer, A. Hofmann, M. Schiefer, and T. Zemen, "Active reconfigurable intelligent surface for the millimeter-wave frequency band: Design and measurement results," in *2024 IEEE Wireless Communications and Networking Conference (WCNC)*, 2024, pp. 1–6. DOI: 10.1109/WCNC57260.2024.10571022.

[27] S. Alamdar, S.-W. Tam, S. Bagherkhani, *et al.*, "A 16 × 16 array composed of 4 × 4 fully scalable reconfigurable intelligent surfaces (ris) for 2.4 ghz wi-fi using rfid distributed control," *IEEE Transactions on Microwave Theory and Techniques*, pp. 1–14, 2025. DOI: 10.1109/TMTT.2025.3547686.

[28] M. Kerbler, “Control unit for a reconfigurable intelligent surface,” Bachelor’s Thesis, TU Wien, Vienna, AUT, 2022.

[29] F. A. Kiss, “Measurement and characterization of a reconfigurable intelligent surface with an automated measurement environment,” Master’s Thesis, TU Wien, Vienna, AUT, 2022.

Symbols and abbreviations

RIS	reconfigurable intelligent surface
IRS	intelligent reflective surface
ITS	intelligent transmitting surface
RTA	reflectarray antenna
TMA	transmitarray antenna
SDM	software-defined metasurface
FPGA	field programmable gate array
LIS	large intelligent surface
SINR	signal-to-interference-plus-noise ratio
AF	amplify-and-forward
DF	decode-and-forward
IoT	Internet of Things
CSI	channel state information
AWGN	additive white Gaussian noise
SNR	signal-to-noise ratio
LOS	line-of-sight
FET	field effect transistor
RFID	radio-frequency identification
VNA	vector network analyzer
DAC	digital-to-analog converter
MCU	micro-controller unit
SPI	serial peripheral interface
PCB	printed circuit board
SMD	surface-mounted device

HF	high frequency
DIG	direct immersion gold
ENIG	electroless nickel immersion gold
ENEPIG	electroless nickel electroless palladium immersion gold
USB	universal serial bus

List of appendices

A RIS module schematic

This appendix includes the schematic of the RIS module. First, there is the overall schematic of how the individual cells are connected to the main pin connector `J1`. The second page then shows the connections of the diodes to their respective group connector `I-IX`. The shown capacitors are not currently used (not soldered on the board) and serve as a precaution if HF shorting becomes necessary in the future.

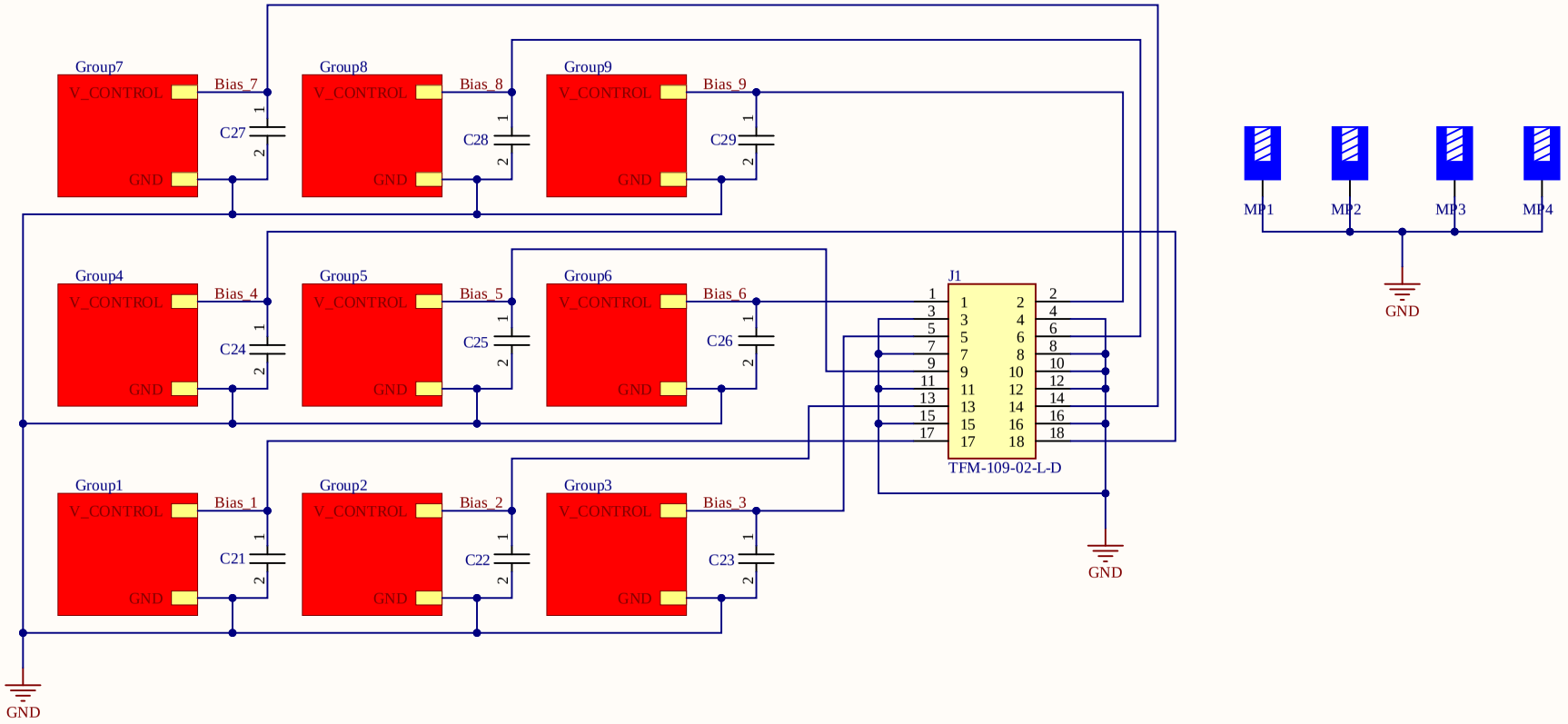

Title			
Size A4	Number		Revision
Date:	5.13.2025	Sheet of	
File:	C:\Users\..\Overall_schematic.SchDoc	Drawn By:	

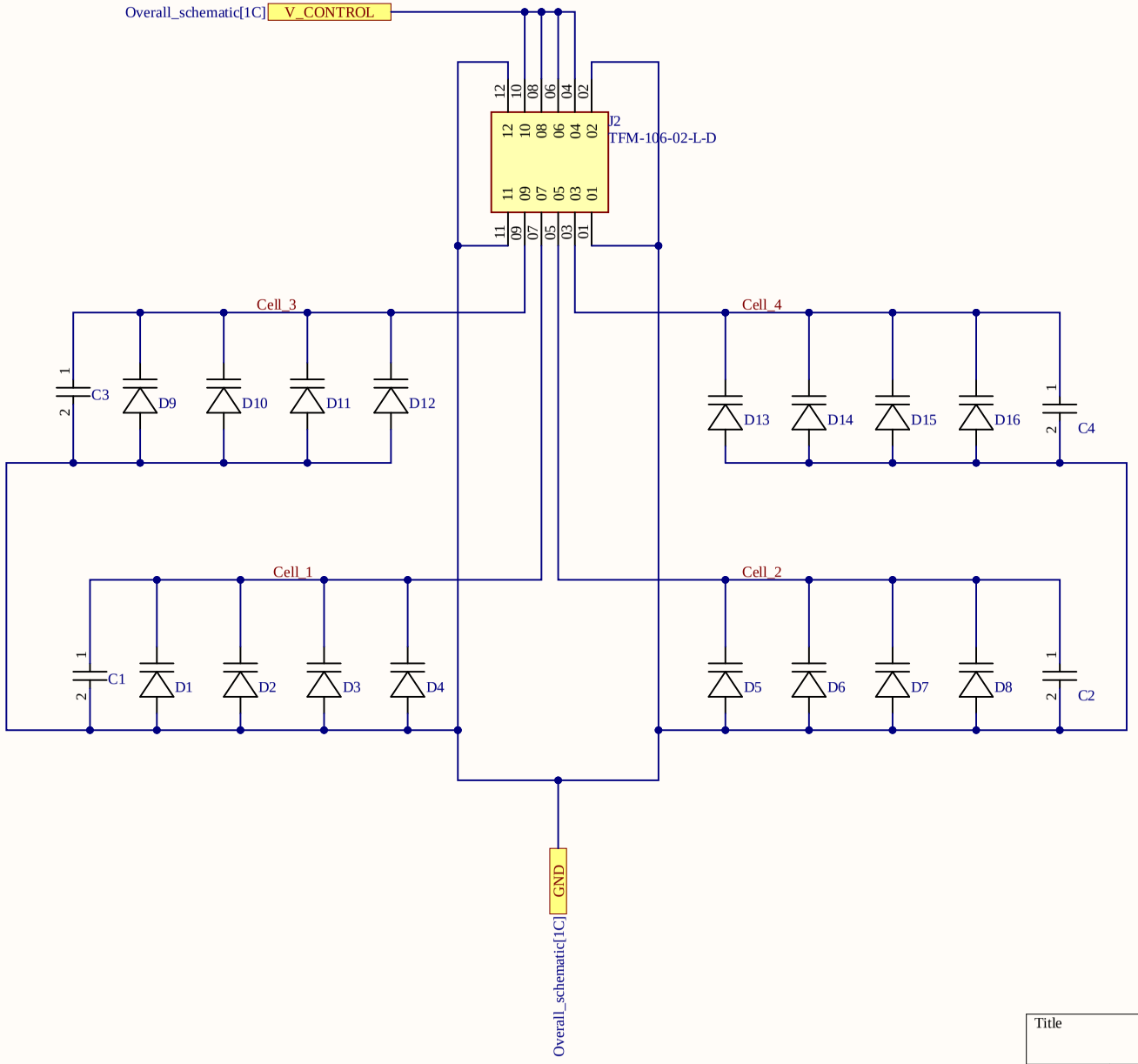

Title			
Size A4	Number		Revision
Date:	5.13.2025	Sheet of	
File:	C:\Users\..\RIS_cell_group.SchDoc	Drawn By:	